Gholami Haghighi Fard, Morteza; Hostikka, Simo

Combustion characteristics of non-charring polymer cylinders - experimental and numerical study

Published in:
Combustion and Flame

DOI:
10.1016/j.combustflame.2022.112587

Published: 01/03/2023

Document Version
Publisher's PDF, also known as Version of record

Combustion and Flame 249 (2023) 112587

Contents lists available at ScienceDirect

Combustion and Flame

journal homepage: www.elsevier.com/locate/combustflame

Combustion characteristics of non-charring polymer cylinders - experimental and numerical study

Morteza Gholami Haghighi Fard, Simo Hostikka*

Department of Civil Engineering, School of Engineering, Aalto University, Finland

ARTICLE INFO

Article history:
Received 3 March 2022
Revised 28 November 2022
Accepted 12 December 2022

Keywords:
PMMA
Cone calorimeter
FDS
Cylindrical fuel
Radiative flux
Convective flux

ABSTRACT

Polymeric fuels with a cylindrical shape are widely found as forest combustibles, building components, and electrical cables and wires. Their flammability is commonly assessed using cone calorimetry, despite the fact that the exposed heat flux is well defined only for flat samples. This has led to great difficulties when trying to use the experimental data for calibrating pyrolysis models, which often treat the problem as one-dimensional. This study aims at increased understanding of the combustion of cylindrical fuels in cone calorimeter by carrying out experiments and two-dimensional numerical simulations on black, 20 mm diameter Poly(methyl methacrylate) rods. The solid-phase heat transfer and pyrolysis are modeled using a rectilinear 1 mm mesh, and the reactive flow field is solved by LES and a single-step mixing-controlled combustion reaction. The model is validated with the results of the gasification and flaming experiments with one or five rods under 50 kW m^{-2} irradiation. For the single rod measurements, a steep vertical shrinkage in gasification, and roughly equal vertical and horizontal degradation rates in flaming were observed. Degradation patterns of the five rods experiments consisted of a ∪-shape trend in gasification, and a ∩-shape trend in flaming condition. The numerical simulations reproduce these deformation trends with a favorable accuracy for all cases. The ignition delay time of the five rods case was detected shorter than the single rod case, which is in consistency with the available literature. The model allowed for the extraction of comprehensive thermodynamic information on the surface of the samples. With flaming, the incident heat flux at the top of the sample increased by 15 kW m^{-2}. Flame-induced convective heating is most significant on the sides of the single rod case or on the outermost rods in the five rods case, with a distribution that peaks to about 30 kW m^{-2}. The current framework can be a basis for extension to modelling more complex cylindrical material such as cables and thermal insulations.

1. Introduction

Throughout the past few decades, vast attention has been given to assessing the flammability of polymers. The great extent of the work has been devoted to slabs and flat geometries due to their omnipresence. In spite of that, polymeric materials in the cylindrical configuration are dominant fuels in many household, industrial, aeronautical, and wildland fire scenarios. Clear Poly methyl methacrylate (PMMA) in a cylindrical shape is widely used in the building industry for the sake of aesthetics [1], and the coverings of electrical wires and cables can be considered as cylindrical thermoplastics and thermosets. Almost 5% of residential fires are initiated by wire and cable ignition [2], while the second most frequent ignited material (after oil) in Nuclear Power Plants is reported to be cable insulation in 21% of fires originated from electrical failure [3]. Similarly, flame propagation on the wiring systems poses a significant fire hazard in aircrafts [4] as well as space explorations [5,6]. For example, the flame blowoff and quenching in microgravity condition on cylindrical PMMA rods were investigated recently [7] in the International Space Station. Regarding forest fires, dead woody shrubs, twigs, and pine needles are the major polymeric combustibles [8,9], which mainly possess a cylindrical structure.

The flammability of polymeric materials is commonly studied by following a hierarchy. Firstly, micro-scale decomposition measurements, such as Thermo-Gravimetrical Analysis (TGA), are used to determine the temperature, form, and kinetics of the pyrolysis reactions. Gram-scale experiments, such as the cone calorimetry measurements [10], are employed to measure the rates of mass loss and heat release. These micro- and gram-scale measurements

* Corresponding author.
E-mail addresses: morteza.gholamihaghighifard@aalto.fi (M. Gholami Haghighi Fard), simo.hostikka@aalto.fi (S. Hostikka).

https://doi.org/10.1016/j.combustflame.2022.112587

are then used to support efforts for analytical, empirical, or numerical modelling of the material pyrolysis. In most of the calorimetry studies performed on polymers, the sample has been a flat slab, cut from the original material manufactured in the form of large sheets, e.g., [11–17], but attempts with different geometries have been made both in research [18] and product classification [19].

Regarding the numerical modeling of polymeric slabs under cone calorimetry, a number of algorithms have been adopted in the literature to present identical conditions and geometry of the problem. Tsai and colleagues [20] adopted a two-dimensional axisymmetric model for the geometry of a PMMA slab exposed to a standard cone calorimeter. The gas phase flow was assumed laminar, while the solid phase degradation was approximated with a quasi-one-dimensional solution. The solid phase solution neglected both the heat of vaporization and the alteration of the slab thickness. Simplifications implemented to the model restrict its applicability to an extent that simulations are reliable only until sample ignition, after which drastic flow divergencies lead to unreliable results. A similar approach has been taken by Brescianini et al. [21], but with three-dimensional modeling of the complete geometry. Although this model showed a very good prediction of pilot ignition times, negligence of flame radiative feedback to the sample and laminar flow assumption in their method still prevented the model functionality beyond the ignition moment.

Very few attempts were made to characterize the fire performance of polymeric cylindrical objects. Hernandez et al. [22] studied the time to ignition for vertically oriented clear PMMA cylinders with diameters of 6.4–12.7 mm in a radiation apparatus. They derived an analytic solution for ignition delay time prediction. The ignition risk of clear PMMA in the form of half-cylinder rods exposed to a horizontal irradiation panel was studied by Tao et al. [1]. To mimic fuels in wildland fires, Lin et al. [23] investigated piloted ignition measurements for cylindrical wood rods in the cone calorimetry scenarios. Nevertheless, the major part of the research on calorimetry of the polymeric cylindrical fuels has been focused on providing experimental [24–28], or combined experimental and analytical [29,30] descriptions for fire behavior of electrical cables and wires. In [23,29,30], a unique survey has been performed on the consequence of varying the layout of the cylindrical fuels on the sample holder of a cone calorimeter. They experimentally discovered that there is a significant effect on the overall combustion performance whether the cylindrical rods were tightly aligned next to one another, or departed far from each other. The underlying thermodynamic reasons have remained unjustified so far, but the recent advances in numerical models have the potential to clarify this phenomenon.

Several computational frameworks have been developed to model the calorimetry measurements. For instance, Gpyro [31], the solid-phase model of the Fire Dynamics Simulator (FDS) [32], and ThermaKin [33] are often employed as pyrolysis solvers to model calorimetry measurements of polymers. In these modeling tools, a transient conduction and radiation heat transfer coupled with the chemical degradation of the fuel is solved. Numerical modeling of cylindrical polymeric objects under the cone calorimetry scenarios is restricted to a limited number of studies. Works of Matala [34], Hostikka and Matala [18,35,36], and Hehnen et al. [37] employed FDS for the simulation of polymeric layers of electrical cables. These studies were carried out by implementing a series of simplifying assumptions: (I) The cylindrical geometry of the sample under cone calorimetry was depicted into a rectangular column comprised of corresponding material volume; (II) The radiative heat, emitted from the conical elements and absorbed on the sample surface, was simply modeled as virtual exposure applied to the flat faces of the rectangular column; and (III) Pyrolysis reactions and heat conduction within the solid phase were assumed to be one-dimensional throughout the thickness of the solid column. Such models cannot capture the processes that arise from the curved shape. For example, the sample area exposed to radiation may be changing over time, and the convective heat transfer over cylindrical bodies is different from that over a flat surface. The simplifications may thus introduce uncertainties that mask the pyrolysis behaviors resulting from the material characteristics and geometrical details, such as the different layers of polymers.

Quite often, the numerical simulations of cone calorimetry (or similar experiments) need to be computationally inexpensive to enable their use as a part of the optimization process to estimate the model's parameters. As the speed is commonly achieved by strong geometrical simplifications and low numerical resolution, the numerical models cannot resolve neither the detailed radiator geometry, nor the flame heat feedback to the sample. For the simulations of flat samples, homogeneous radiator irradiance can be assumed, and empirical models can be applied for the flame heat fluxes. However, almost no methods exist for measuring heat fluxes on the surfaces of cylindrical samples. Hence, the necessary information must be obtained through detailed numerical simulations, which is the main motivation of the current work. This study targets for (a) characterizing the flammability of cylindrical polymer objects under cone calorimetry, (b) implementing a detailed modeling framework that can resemble the nature of the problem in a more realistic manner, and (c) providing robust support for the interpretation of the cable test results, to achieve a perception that can be used in the simplified models. Hence, the current work investigates the fire performance of non-charring polymeric rods with cone calorimeter firstly with experiments. The cone calorimeter tests provide reference mass loss and energy release of the samples, and measurements are recorded with a thermal camera to supply material shrinkage data. A numerical methodology is employed to simulate the problem, which serves as the tool for obtaining comprehensive thermophysical data in the vicinity of the samples. This numerical framework is constructed with a two-dimensional resemblance of the actual geometry of the conical heater and cylindrical objects, while the solid phase solution is based on two-dimensional pyrolysis and heat transfer implementations. After validating the methodology, the numerically obtained distribution of the thermal data on the rods is used to explain the observed shrinkage patterns.

2. Experimental methods

2.1. Material selection

PMMA is widely used as reference material in flammability studies because of its well characterized properties and good repeatibility of its pyrolysis behavior [38,39]. Models involving condensed-phase pyrolysis are often validated with experiments performed on reference materials like PMMA, for example [13,40–44]. In this study, cast black PMMA in the form of rods with a measured diameter of 20 ± 0.1 mm, manufactured by Aikolon, was utilized. The sample had a measured density of 1196 ± 2 kg m^{-3} in room temperature. To prepare material for TGA tests, a small section of the sample was cut by a circular saw, crushed into smaller particles with a milling machine, and further powdered via a mortar until fine grains of the material were obtained. The samples for cone calorimetry experiments were cut from the original rods into pieces of 95 ± 1 mm length with a circular sawing machine.

2.2. Milligram-scale experiments

Thermogravimetric analysis was performed using a Netzsch Simultaneous Thermal Analyzer (STA) 449 F3 Jupiter to characterize the reaction kinetics. The powdered sample was heated in an

Aluminum Oxide crucible without a lid. An inert environment was established inside the furnace via continuously purging it with Nitrogen at a rate of 50 cm^3 min^{-1}. The sample underwent a heating program described as follows. Firstly, the material was heated to 315 K and preserved at this temperature for 20 minutes to obtain an equilibrium condition. Subsequently, a heating rate of 10 K min^{-1} was applied, increasing the sample temperature until 873 K. A baseline test with an empty sample and reference crucible was performed with the same heating program at the beginning of the tests as the correction data. The TGA tests were repeated five times. Each test was performed with samples weighing 4–7 mg.

2.3. Gram-scale experiments

The flammability of the PMMA rods was examined by an ISO 5660 cone calorimeter with a custom sample chamber under gasification as well as flaming conditions. In gasification measurements, the test chamber was continuously purged with Nitrogen so that the volumetric Oxygen concentration inside the chamber was measured to be less than 1%. During the flaming experiments, the chamber doors were open to the laboratory to enable easier thermal imaging.

All measurements were carried out at 50 kW m^{-2} radiative heat flux. The nominal heat flux was calibrated with a fluxmeter at the standard position of 25 mm away from the cone plate. This position corresponds to the top surface of the central rod placed on the sample holder. Two sets of experiments were performed: (1) placing only a single PMMA rod in the middle of the sample holder, and (2) placing five rods next to each other to fill all 10 cm × 10 cm-area of the sample holder. The mass loss rate (MLR) and heat release rate (HRR) were recorded until all of the material had burned away. For most configurations, three repeated tests were carried out. The results are presented as arithmetic means and 95% confidence limits, calculated as two times the time averaged standard deviations and expanded on smoothed (10-point moving average) mean curves.

Videos were recorded from the cross-sectional degradation of the samples using a thermal camera (FLIR A655sc). Recording of the closed chamber during the gasification tests was facilitated by the use of a Calcium Fluoride Crystal window (FLIR IRW) installed on one of the glass doors of the chamber. To interpret the camera readings while using the IR window, a temperature-dependent calibration for the transmissivity was used. Extracted images from the videos served as the reference for a qualitative comparison against model results for material shrinkage.

3. Numerical methods

The numerical simulations were performed using the FDS [32] software (release version FDS6.7.6), which is a computational fluid dynamics solver for fire-driven flows. It solves the weakly-compressible Navier Stokes equations with a single-step, mixing-controlled combustion model, a Finite Volume Method (FVM) for thermal radiation, and separate models for condensed-phase heat transfer and decomposition reactions. This section describes the employed condensed-phase algorithms and summaries of the radiation and combustion models. The reader is referred to [32] for details of each algorithm denoted herein.

3.1. Pyrolysis reaction model

The pyrolysis reaction model within the solid material is based on the conservation of mass between the gaseous species and the condensed materials. For a given material component α, the time evolution of local density ($\rho_{s,\alpha}$) is solved by:

$$\mathrm{PMMA} \xrightarrow[A_{11},\,E_{11},\,n_{s,11}]{r_{11}} \begin{cases} (94\,\%)\ \text{Intermediate PMMA} \xrightarrow[A_{21},\,E_{21},\,n_{s,21}]{r_{21}} \text{MMA gas} \\ (6\,\%)\ \text{MMA gas} \end{cases}$$

Fig. 1. Modeled degradation path of the material under study.

$$\frac{\partial}{\partial t}\left(\frac{\rho_{s,\alpha}}{\rho_s(0)}\right) = -\sum_{\beta=1}^{N_{r,\alpha}} r_{\alpha\beta} + S_\alpha \tag{1}$$

where $\rho_s(0)$ is the initial material density, $N_{r,\alpha}$ is the number of reactions for material α, $r_{\alpha\beta}$ is the rate of reaction β, and S_α is the production rate of component α due to the reactions of the other components. The reaction rate, $r_{\alpha\beta}$, is calculated based on Arrhenius function:

$$r_{\alpha\beta} = A_{\alpha\beta}\left(\frac{\rho_{s,\alpha}}{\rho_s(0)}\right)^{n_{s,\alpha\beta}} \exp\left(-\frac{E_{\alpha\beta}}{RT_s}\right) \tag{2}$$

where $A_{\alpha\beta}$ is the pre-exponent factor, $E_{\alpha\beta}$ is the activation energy, and $n_{s,\alpha\beta}$ is the reaction order of the reaction β of the component α. R and T_s are the universal gas constant and solid temperature, respectively. Note that we assume no gas diffusion inside the condense phase.

Thermogravimetric measurements of PMMA in inert atmosphere indicate a main decomposition reaction with a peak reaction rate between 350 and 370 °C [45–48]. Another, lower reaction peak is sometimes observed at lower temperatures, with onset temperature between 130 to 260 °C. Engineering models of PMMA pyrolysis commonly focus on the main reaction and describe the process using a single reaction [13,40,43], but two-step reactions have also been publised to include the lower-temperature reaction [39,42].

TGA measurements with the current material showed that the first reaction accounts for 6% wt of total mass loss. As this result is close to the observation of Fiola et al. [42], we adopt a similar two-step consecutive reaction model as in [42]. The reaction path and corresponding kinetic parameters are illustrated in Fig. 1. The values of the kinetic parameters were optimized by simulating a non-oxidative TGA experiment at 10 °C min^{-1} heating rate. This heating rate was selected to maintain an iso-thermal condition and avoid intense temperature and concentration gradients on the samples, hence preventing thermal decomposition kinetics and energetics from the transience that would be caused by heat and mass transport delay [42]. Initial estimates of the parameter values were obtained with the built-in TGA analysis solver of FDS. The values were then adjusted further to obtain best possible fit for the TGA mass and TGA mass loss rate by visual inspection. The optimal parameter set is $A_{11} = 1.02 \times 10^{12}$ s^{-1}, $E_{11} = 1.32 \times 10^5$ kJ mol^{-1}, $n_{s,11} = 3.0$, $A_{21} = 9.43 \times 10^9$ s^{-1}, $E_{21} = 1.47 \times 10^9$ kJ mol^{-1}, $n_{s,21} = 1.0$. The parameter values are model-dependent, however, the obtained values are within the ranges reported in the literature [40].

Figure 2 compares the measured and simulated TGA mass (Fig. a) and mass loss rate (Fig. b) at 10 °C min^{-1} heating rate. The model accurately reproduces the current measurement in terms of mass loss amplitudes and timings of both reactions. To understand how representative the current results are for PMMA materials in general, we compare the current results against a data set collected during an international MaCFP (Measurement and Computation of Fire Phenomena work group) round-robin [49]. The MaCFP data set is an average of TGA measurements from 11 participating institutions. The decomposition behaviors of the current and MaCFP materials are found to be very similar. The main difference is the 9.4 °C shift of the main decomposition peak towards higher temperatures in MaCFP data. Considering the fact that the sample ma-

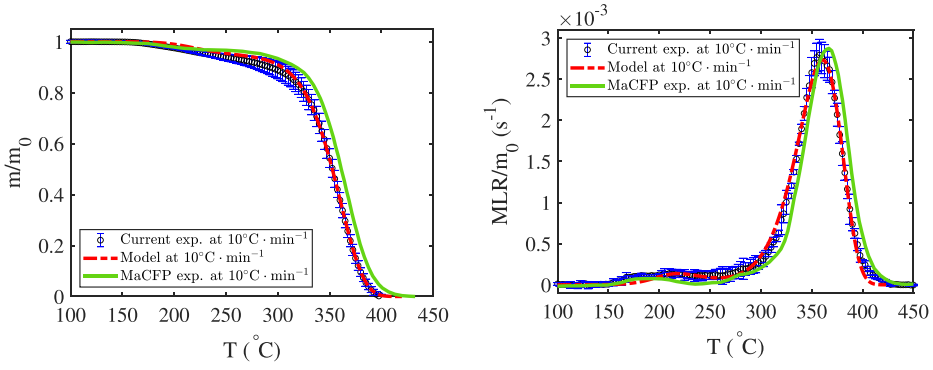

(a) Normalized TGA mass (b) Normalized TGA mass loss rate

Fig. 2. Comparison of measured and simulated (using optimized kinetics) thermogravimetric analysis of the PMMA under study against a reference data [49] for heating rate of 10 °C min^{-1}.

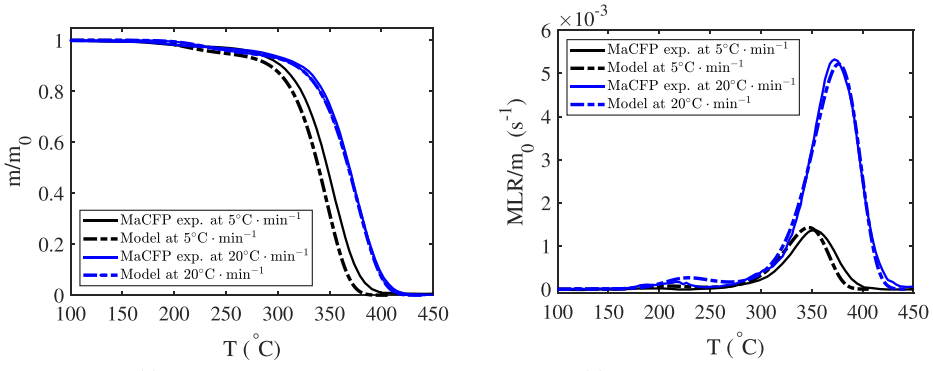

(a) Normalized TGA mass (b) Normalized TGA mass loss rate

Fig. 3. TGA model performance in 5 and 20 °C min^{-1} heating rates. The kinetic parameters used in the simulations are the ones optimized for the 10 °C min^{-1} heating rate.

terials were obtained from different sources, the generality of decomposition model can be considered good.

When exposed to external heating, different positions of the material experience a wide range of different heating rates, and the validity of the kinetic model calibrated at 10 °C min^{-1} heating rate becomes a question. In Fig. 3, we compare the model predictions at 5 and 20 °C min^{-1} heating rates against the corresponding data from MaCFP [49]. At 5 °C min^{-1}, the simulated main decomposition reaction occurs at 6 °C lower temperature than in the test. The comparison at 20 °C min^{-1} shows how the simulated MLR peaks occur marginally later than in the experiment (9.1 °C and 4.6 °C). The deviations can be considered negligible due to the uncertainties stemming from the different polymer sources. The model is thus expected to perform reliably at heating rates other than the calibration test.

3.2. 2D heat transfer algorithm

The solution of heat transfer within the solid material is governed by the Finite Volume -discretization of Eq. (3). On the left-hand side of this equation, ρ_s, c_s, and T_s denote density, specific heat, and the mean temperature of a solid cell, respectively. The right-hand side contains the divergence of the heat flux vector, $\dot{\mathbf{q}}''$, and the volumetric heat source term due to pyrolysis reactions, $\dot{q}'''_s$.

$$\rho_s c_s \frac{\partial T_s}{\partial t} = -\nabla \cdot \dot{\mathbf{q}}'' + \dot{q}'''_s \tag{3}$$

The heat flux vector at the center of cell faces is computed from the first-order discretization of Fourier's law in each coordinate. Consider the x direction with cell indices i and $i+1$, and their corresponding face center $i+\frac{1}{2}$. The intercell flux at time level n is

$$\dot{q}''_{x,i+\frac{1}{2}} = -k_{s,i}\frac{T^n_{s,i+\frac{1}{2}} - T^n_{s,i}}{\frac{1}{2}\delta x_i} = -k_{s,i+1}\frac{T^n_{s,i+1} - T^n_{s,i+\frac{1}{2}}}{\frac{1}{2}\delta x_{i+1}} \tag{4}$$

where k_s is the thermal conductivity. The temperature of the cell interface is calculated via

$$T^n_{s,i+\frac{1}{2}} = \frac{T^n_{s,i} + \left[\frac{k_{s,i+1}}{k_{s,i}}\frac{\delta x_i}{\delta x_{i+1}}\right]T^n_{s,i+1}}{1 + \left[\frac{k_{s,i+1}}{k_{s,i}}\frac{\delta x_i}{\delta x_{i+1}}\right]} \tag{5}$$

However, when material is consumed, δx distances are reduced. Consideration of the changing volume on the Eulerian grid is challenging. Figure 4 shows how the reduced cell distances $\delta\tilde{x}$ and $\delta\tilde{z}$ are stored within the fixed Eulerian grid. Values of $\delta\tilde{x}$ and $\delta\tilde{z}$ are tracked by the pyrolysis solver using a parameter called *solid cell area ratio*, ϕ_s, as explained in the next section. The intercell heat flux with material deformation is approximated by Eq. (6) as an example for the cell "$i, k-1$":

$$\dot{q}''_{x,i+\frac{1}{2},k-1} \approx -k_{i+\frac{1}{2},k-1}\frac{T^n_{s,i+1,k-1} - T^n_{s,i,k-1}}{\frac{1}{2}(\delta\tilde{x}_{i,k-1} + \delta\tilde{x}_{i+1,k-1})} \tag{6}$$

The boundary condition on the outer surface of a solid obstruction is the continuity of heat fluxes:

$$-k_s\frac{\partial T_s}{\partial x} = \dot{q}''_r + \dot{q}''_c \tag{7}$$

where $\dot{q}''_r$ is the net radiative and $\dot{q}''_c$ is the convective flux. In-depth radiation is modeled by calculating the solid's thermal conductivity as a sum of temperature dependent Fourier conductivity $k(T_s)$ and "radiative conductivity", based on the optically thick ap-

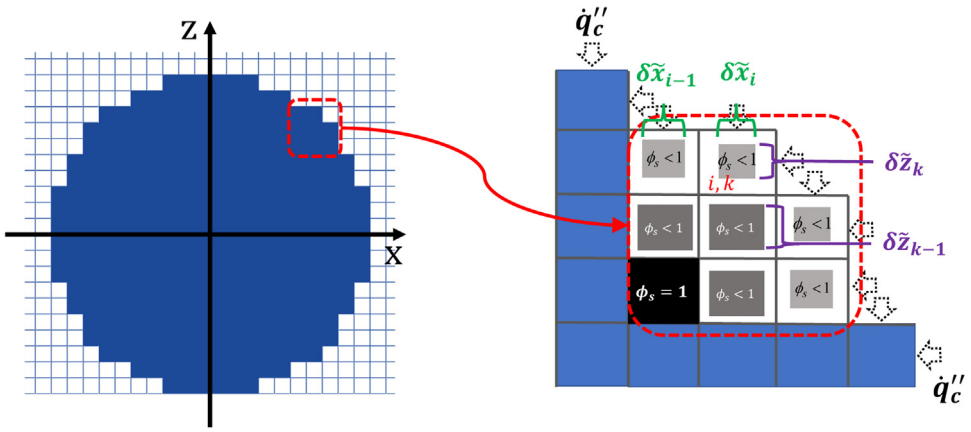

Fig. 4. The Cartesian surrogate of the cylindrical object (left) and shrinkage of a part of the material after a while (right). Gray and black rectangles show the solid cell area ratio, ϕ_s, for the selected region. Dotted arrows represent convective heat flux.

proximation [50]:

$$k_s(T_s) = k(T_s) + \frac{16 n_s^2 \sigma T_s^3}{3\kappa_s} \tag{8}$$

where n_s is the refractive index, σ is the Stefan–Boltzmann constant, and κ_s is the absorption coefficient of the solid.

The convective heat flux is calculated as $\dot{q}''_c = h(T_g - T_w)$, where T_g is the gas temperature in the center of the first off-wall gas-phase cell and T_w denotes the wall surface temperature. The heat transfer coefficient, h, is based on a combination of empirical correlations for the natural and forced convection [32,51]:

$$h = \max\left[\, C|T_g - T_w|^{\frac{1}{3}} \,,\ \frac{k}{L}\mathrm{Nu} \,,\ \frac{k}{\delta n/2} \,\right] \quad \mathrm{W/(m^2\ K)} \tag{9}$$

where L is a characteristic length scale $L = 10$ cm, Nu is the Nusselt number depending on the geometrical and flow characteristics, δn is the normal grid spacing, and C is an empirical coefficient for natural convection (1.52 for a horizontal plate and 1.31 for a vertical plane [51]). The convective flux is applied to the horizontal and vertical surfaces of the solid cell boundaries that are in contact with the gas phase, as shown by dotted arrows in the right side of Fig. 4. For details of discretization of the boundary condition, the reader is referred to the FDS Technical Reference Guide [32].

3.3. 2D pyrolysis algorithm

Solid PMMA is comprised of a mixture of two components, PMMA and Intermediate PMMA. The density of the α's component is material mass divided by the material volume i.e., $\rho_\alpha \equiv m_\alpha / V_\alpha$. The bulk density of the component α of the solid s is defined as $\rho_{s,\alpha} \equiv m_\alpha / V_s$, where its time evolution is solved by Eq. (1).

The key feature of the 2D pyrolysis model is the technique used for handling material deformation. Since the solid mass is bound to the 2D computational grid, the mesh cells cannot vanish when a material burns away. On that account, the ratio (ϕ_s) between the solid area (solid volume in case of 3D simulations) and the local cell area (volume in 3D) is continuously tracked by:

$$\phi_s \equiv \frac{A_s}{A_{\mathrm{cell}}} = \frac{\sum_\alpha A_\alpha}{A_{\mathrm{cell}}} = \sum_\alpha \frac{m_\alpha/\rho_\alpha}{m_\alpha/\rho_{s,\alpha}} = \sum_\alpha \frac{\rho_{s,\alpha}}{\rho_\alpha} \tag{10}$$

The material deformations is assumed to be isotropic, meaning that it deforms identically in both x and z directions. The deformed solid cell dimensions are thus calculated as:

$$\delta\tilde{x}_i = \phi_s^{1/2}\delta x_i \tag{11}$$

where $i = 1$ for x, and $i = 2$ for z direction. Figure 4 demonstrates a schematic of solid cell area ratio, ϕ_s, and the corresponding new *virtual* cell dimensions, $\delta\tilde{x}$ and $\delta\tilde{z}$. In the figure, the gray cells represent locations that have already initiated evaporation, thus having $\phi_s < 1$. Pyrolysis reactions can occur both at and below the surface. Cells deeper inside the object, such as the black cell in Fig. 4, can be still filled with the virgin material and have $\phi_s = 1$. As the solid cells on the surface pyrolyze completely ($\phi_s \to 0$) and vanish, the place of the thermal boundary condition needs to be updated. To avoid numerical problems at $\phi_s \to 0$, the burn-away of a cell is assumed when its mass falls below 10% of its initial value. The remaining mass is then allocated to an adjacent solid cell. These sudden changes in solid and flow geometries (solid mesh is utilizing the same mesh as the flow solver) are found to cause some fluctuations in the pyrolysis rate, but the flow simulations remain stable due to the automatic time step control. The burn-away of the cylinder's last cell takes place at $\phi_s = 10^{-6}$.

Almost all materials show resistance to gas transport from the depth to the surface, but modeling the porous flow is very demanding. In this work, transport of the pyrolyzed gas is considered instantaneous, assuming infinite permeability. The pyrolyzed mass is ejected from the nearest solid wall cell and the isotropic deformation model is applied. In 2D, a wall cell may be assigned for the ejection of pyrolyzed gas produced by more than one solid cell below its surface (see Fig. 4). Therefore, the mass flux of that given wall cell is computed via summation of the pyrolyzate generation over the row or column of solid cells linked to it. For example, the mass flux generation of pyrolysis gas component γ for a row of cells in the x direction linked to wall cell w is calculated by Eq. (12):

$$\dot{m}''_{\gamma,w} = \sum_{i\in w} \dot{m}'''_{\gamma,i,k}\,\delta x_i \tag{12}$$

where $\dot{m}'''_{\gamma,i,k}$ is the rate of mass generation per unit area for the pyrolyzate component γ.

3.4. Radiation and combustion models

Thermal radiation in the gas phase is solved using the Finite Volume Method (FVM) for radiation, assuming gray, non-scattering gas. Narrow-band model RadCal is used at the beginning of each simulation to generate lookup tables of temperature dependent gray absorption coefficients for all participating gases (fuel, water vapor, carbon dioxide) + soot. During the simulation, absorption coefficients are fetched from the tables and added up according to the instantaneous volume fractions within each cell. The spatial discretization of the radiation transport equation utilizes the CFD mesh, and the solid angle is divided into 60 control angles [32]. In

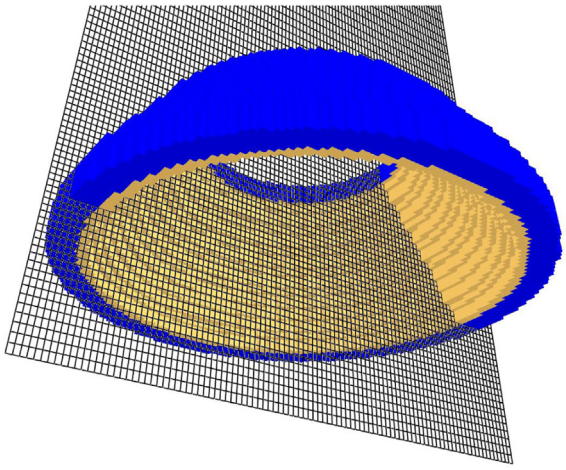

(a) Full 3D cone model used in Ref. [54].

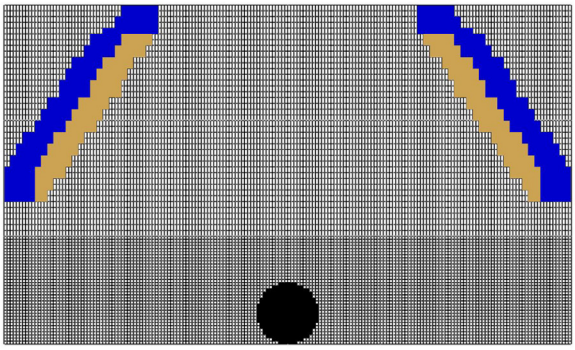

(b) A vertical plane passing through the full 3D geometry.

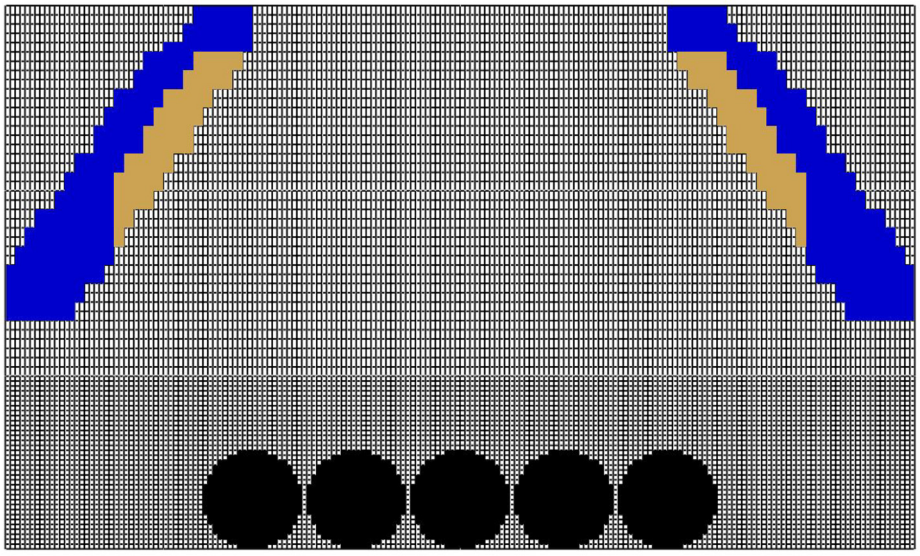

(c) The modified 2D cone heater geometry.

Fig. 5. Adjustments performed to set up the 2D cone heater model: (a) The original full 3D model from Ref. [54]; (b) A vertical plane passing midway through the 3D cone geometry, along with the presence of a single PMMA rod; (c) The modified 2D cone heater geometry used in the current study, along with the presence of five PMMA rods. Displaying PMMA rods here is only intended for giving an insight to the reader about the interior of the solution domains.

the calculation of the emission source terms, we assumed that the temperature field is well resolved by the 1 mm mesh size.

For combustion reaction, an infinitely-fast chemistry model is utilized [52]. At the start of a time step, each computational cell has an initial concentration of species (reactants, products, and inert gases) that exist with some degree of mixing. The chemical mass consumption rate of fuel, $\dot{m}'''_F$, is calculated using the Eddy Dissipation Concept [52]:

$$\dot{m}'''_F = -\rho \frac{\min(Y_F, Y_A/s)}{\tau_{mix}} \tag{13}$$

where ρ is the cell mass density, Y_F and Y_A are the cell mean mass fractions of Fuel and Air, respectively, and s is the mass stoichiometric coefficient for air. Characteristic mixing time, τ_{mix}, is based on the local state of the flow field, taking into account the time scales required for chemical reactions, molecular diffusion, subgrid-scale advection, and buoyant acceleration. Details of the model can be found in [32]. The local heat release rate is then computed by multiplying $\dot{m}'''_F$ by the heat of combustion.

4. Cone calorimetry model setup

A 2D plane passing through the center of the cone heater was modeled. The PMMA cylinder cross-sections were built from 1×1 mm^2 solid obstructions, providing a numerical approximation of the circular shape. The mineral wool substrate beneath the rod was modeled as a horizontal, 10 cm wide non-combustible boundary. For flaming simulations, the surface temperature of the substrate was predicted by solving a one dimensional heat conduction equation with thermal properties $\rho = 128$ kg m^{-3}, $k_s = 0.1$ W m^{-1} K^{-1}, and $c_s = 1$ kJ kg^{-1} K^{-1}, extracted from the product information sheet [53]. In the non-flaming condition, observations from the thermal camera revealed that the wool temperature remains relatively constant. Therefore, fixed temperatures of 450 °C and 200 °C were assigned to wool surface in case of single and five rods simulations, respectively.

The model of the heater was based on an earlier study of Hostikka et al. [54], where a complete 3D model of the conical heater was built with cold outer and hot inner obstructions

Table 1
Thermal parameters used on condensed phase degradation model [31].

Name	k_0 (W/mK)	n_k (−)	c_0 (kJ/kgK)	n_c (−)	ϵ (−)	κ (m^{-1})	H_r (kJ/kg)
PMMA	0.20	−0.19	1.606	0.89	0.86	1980	5 [42]
Intermediate PMMA	0.18	−0.18	1.667	0.72	0.87	1000	728

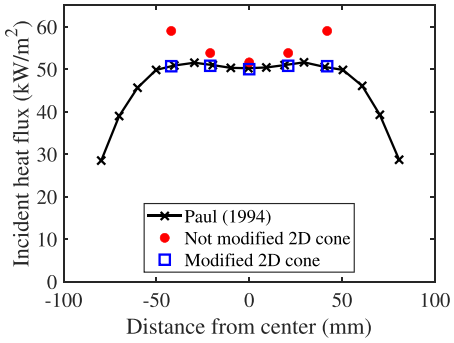

Fig. 6. Comparison of incident heat flux distribution between the unmodified 2D cone heater, the modified 2D cone heater, and the reference [56]. The current fluxes are obtained for points located at the top of each PMMA rod.

(Fig. 5(a)). Vertical plane passing through the original cone geometry, adopted for the 2D model of this paper, is shown in Fig. 5(b). To ensure that the simulated distribution of the incident radiative flux on the sample surface complies with experimental observations [54–56], the heater geometry had to be modified by reducing the width of heater by 12 mm (Fig. 5(c)). Figure 6 shows a comparison of the predicted heat fluxes prior and after the modification, together with the measured data of Paul [56]. The modified heater geometry provides an accurate initial heat flux distribution.

To adequately capture the intense flow divergence, heat transfer, and combustion in the vicinity of the sample rods, the first 35 mm (from the bottom) of the domain was meshed with cell sizes $\Delta x = \Delta z = 1$ mm. In the region of the cone heater, the cell size was $\Delta x = 1$ mm and $\Delta z = 1.875$ mm. The region far above the heater was only needed in the simulation of five rods under the flaming condition to capture the heat release from long flames and was meshed with $\Delta x = 2$ mm and $\Delta z = 1.875$ mm cells. The computational domain was split into 7, 11, and 13 grids in gasification, single rod flaming, and five rods flaming simulations, respectively. To accelerate the calculations, each grid was sent to a separate process using MPI (Message Passing Interface).

All the horizontal and vertical exterior boundaries (except for the location of the wool substrate) were considered as open boundary conditions feeding the domain with air or pure Nitrogen, in the case of flaming or non-flaming simulations, respectively.

The PMMA material model's thermophysical parameters were taken from the literature without any further calibration or tuning. Temperature dependent thermal conductivity $k(T) = k_0(T/T_r)^{n_k}$ and specific heat $c(T) = c_0(T/T_r)^{n_c}$, with reference temperature $T_r = 300$ K, along with the surface emissivity ϵ and in-depth absorption coefficient κ were adopted from the work of Lautenberger et al. [31]. The heat of reaction (H_r) of the first reaction step was adopted from the study of Fiola et al. [42] due to the similarity of reaction schemes. Thermal parameters are summarized in Table 1.

In the gas phase, the combustion of MMA monomer, ejected from the surface of the pyrolyzing rods, was assumed to take place as a single mixing-controlled reaction with ambient air, yielding 1% Carbon Monoxide and 2.2% soot [57] as products of incomplete combustion. The heat of combustion reaction was 22.4 MJ kg^{-1} [56,58]. For the single rod flaming simulation, it was necessary to prevent early ignition by specifying an auto-ignition temperature of 421 °C [59], below which the combustion was not allowed to initiate. Such a setup was not necessary for the five rods flaming case because the experimental ignition time was much shorter than the single rod flaming case, making the difference between simulation and measurements practically insignificant.

5. Results and discussion

5.1. Gasification cone calorimetry

Here, we investigate how accurately the 2D model can predict the mass loss rate of a single or five PMMA rods in gasification experiments. The predicted mass loss rates in the single rod and five rods gasification tests are compared against their corresponding experimental results in Fig. 7. In both cases, the model shows an excellent capability of predicting the time dependency of the material pyrolysis, considering the level of experimental and parameter uncertainties. In the experiments with five rods, some melting of PMMA was observed during the last minutes of the tests. Also, small amounts of material close to the outer sides of the sample holder started disintegrating and tumbling down at about $t = 1000$ s in all tests. Most repetitions were seized at about $t = 1100$ s to prevent any damage to the cone calorimeter parts from melted hot PMMA. The applied numerical model cannot reproduce this disintegration, and we expect this constitutes the main reason for the deviation of model result from the experimental curve from $t = 1000$ s onward in Fig. 7(b). This deviation will be elaborated visually in Section 5.4.

The fluctuations in numerical results originates from the *burn away* feature of the solution. When the PMMA inside a solid cell evaporates completely, the corresponding cell vanishes from solid domain, turning into a gas cell. This relatively sudden cell transformation results in a cyclic behavior as seen in Fig. 7. To decrease the severity of this behavior, one can decrease the mesh resolution in order to cause more smooth transformation. It will be shown in Section 5.3 that simulation with 0.5 mm grid leads to smooth results, although increasing the computational cost drastically.

5.2. Flaming cone calorimetry

Here, we investigate how accurately the 2D model can predict the mass loss rate and heat release rate of a single or five PMMA rods in flaming measurements. The simulated MLR and HRR for the single-rod flaming case are compared against the experimental data in Fig. 8. The model is able to capture the main features of material evaporation and energy release in terms of time-to-ignition, time-to-peak, and trend preservation. The grid size will be discussed more in Section 5.3, but now we can already observe that the 1-mm resolution can yield results that are sufficiently accurate for engineering analyses.

To demonstrate the validity of the 2D approximation, a 3D simulation of the single rod flaming case was performed (Appendix A). The results show that the 2D and 3D results mainly differ in ignition time, a process that was not explicitly modeled, yielding quantatively similar predictions of the post-ignition mass loss rates. The 2D model can be considered sufficiently accurate representation of the 3D problem, while demanding considerably less computational resources.

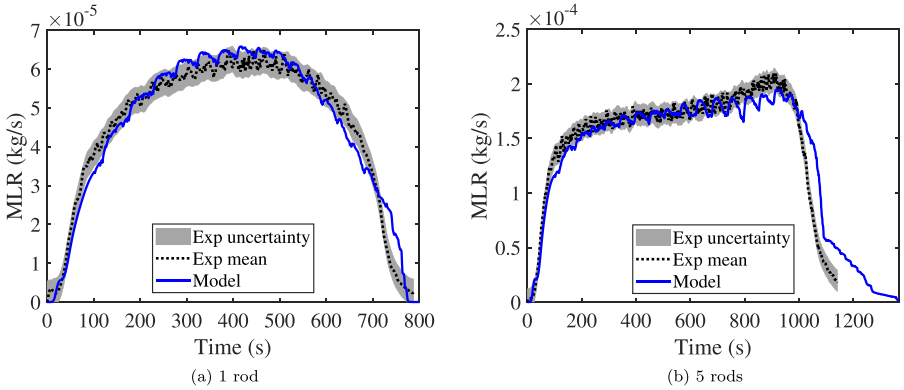

Fig. 7. Comparison of mass loss rates between experimental and model prediction for single and five rods gasification test cases.

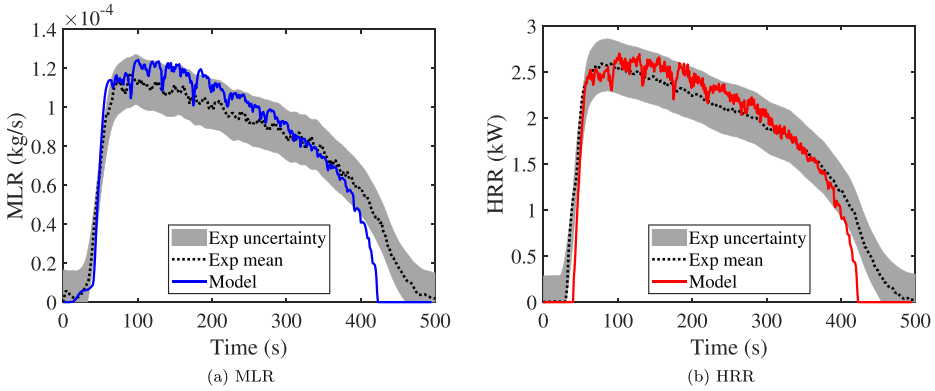

Fig. 8. Comparison of mass loss and heat release rates between experimental and model prediction for single rod flaming test case.

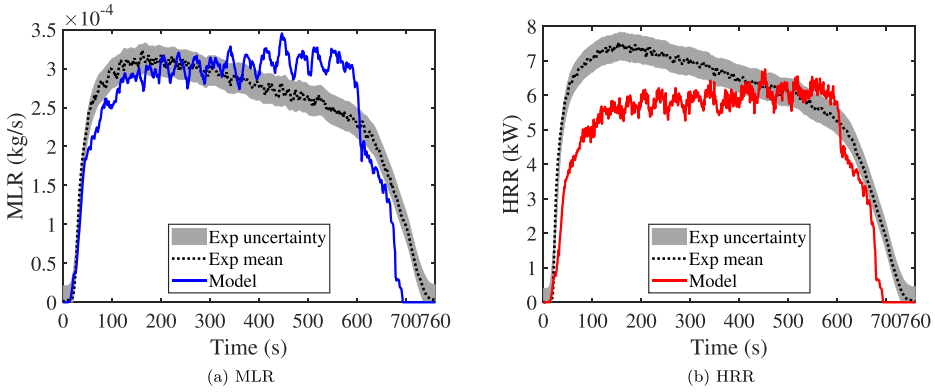

Fig. 9. Comparison of mass loss and heat release rates between experimental and model prediction for five rods flaming test case.

The predicted MLR and HRR of the five rods flaming case are compared against the experimental results in Fig. 9. Here, the differences between the simulated and measured curves are significantly greater than in the gasification tests or the flaming test with just one rod. One prominent difference is the model's increasing trend after ignition, while the experiments retain the decreasing trend in both MLR and HRR. The integrals of the model and the mean experimental MLR curve match with less than 0.1% difference, but there is a 16% difference in the HRR integrals. Regarding the general reliability assessment of the proposed model for flaming situations, one should consider that in flaming conditions, experimental uncertainties are generally higher than in the gasification tests due to the higher sensitivity of the flame-induced heat transfer on the gas phase boundary conditions. On the other hand, we will authenticate a satisfactory shape-change prediction for this test case in Section 5.4. Thus, it can be concluded that the 2D model acceptably simulates the condense phase decomposition based on the heat transfer within, on the surface, and inside the flame capsule encompassing the vicinity of the rods.

Qualitative differences in HRR may partly stem from the flame physics far away from the sample. We did confirm that the simulation domain was tall enough to enable the combustion of all gas phase MMA, but the effects of the reduced numerical resolution towards to top of the domain remain unclear. Intense mixing and rapid flamelet wiggling above the conical heater were observed in the five rods flaming test. Although the 3D simulation did not produce significantly different results for the single rod case, it is possible that the increasing trend of MLR stems from the 2D approximation, which in the five rod case may lead to less accurate turbulent combustion and flame heat feedback. Further evaluation

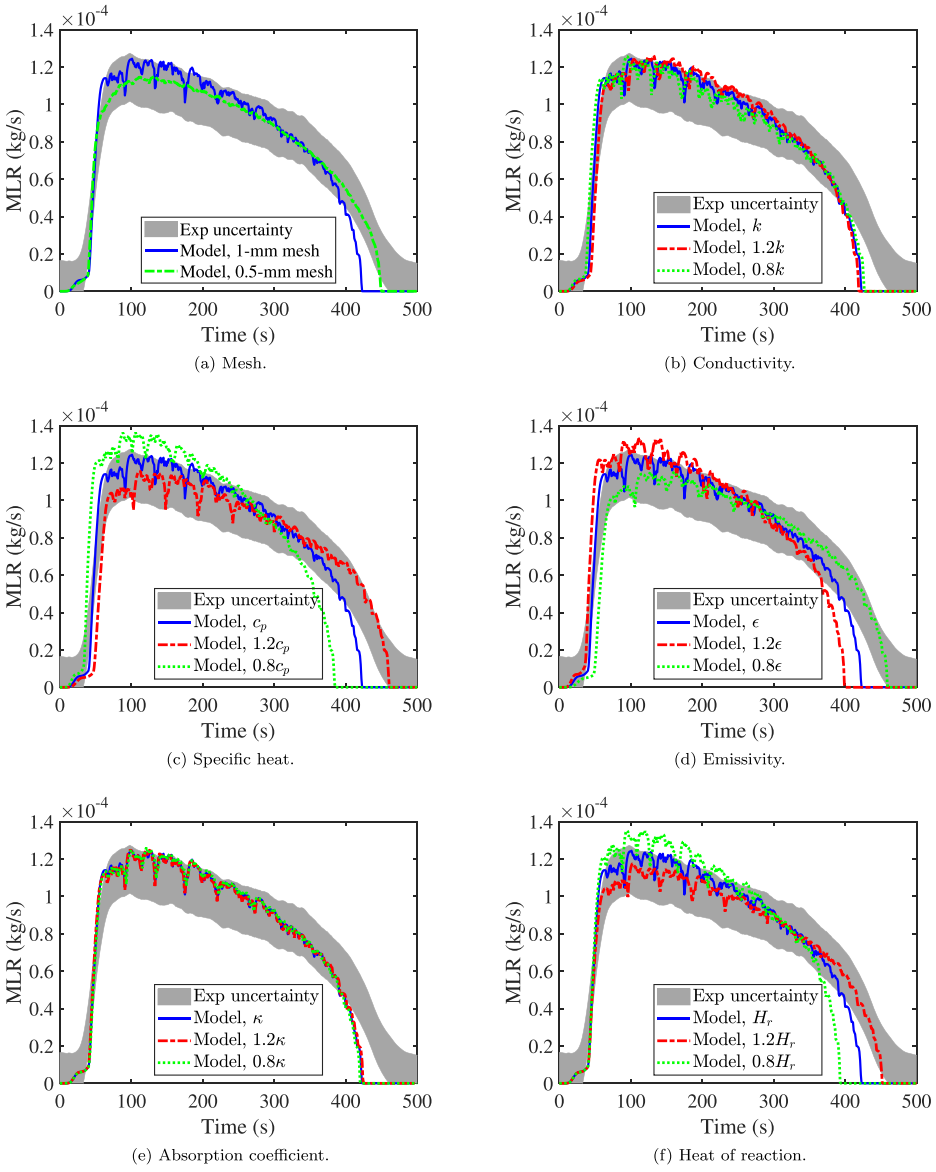

(a) Mesh. (b) Conductivity. (c) Specific heat. (d) Emissivity. (e) Absorption coefficient. (f) Heat of reaction.

Fig. 10. Sensitivity of the single rod flaming MLR for mesh resolution and thermal parameters. In the thermal parameter figures, the model results with the original value (solid lines) are compared against the results with 20% increase of the corresponding parameter (dash-dotted lines) and 20% decrease of that (dotted lines).

of the combustion physics away from the condense phase and 3D turbulent effects can be a matter for future studies.

The cone calorimetry study of Lin et al. [23] considered wooden rods in similar layouts as what was studied here. They observed that the tightly aligned rods next to each other (referred to as fuel bed) ignited faster than a single rod placed in the middle of the sample holder. Same observation can be made from our results by comparing Figs. 8 and 9.

5.3. Model sensitivity

This section assesses the sensitivity of the model to the numerical resolution, the thermal parameters, and the parameters of the convection calculations. All the sensitivity studies were performed for the single-rod flaming case.

To quantify the effect of the mesh resolution, the case was simulated with a 0.5 mm resolution and a new rod geometry with 0.5×0.5 mm^2 solid cells. As a result, the simulation time increased almost fourfold. Figure 10(a) shows the fine-grid result together with the 1-mm result. The 0.5 mm resolution leads to a smoother result due to less abrupt transformation of solid cells into gas cells. The finer resolution is seen to improve the MLR prediction at the end of the experiment by delaying the burnout by 27 s, thus bringing the simulation into the range of experimental uncertainty.

The sensitivity to the angular resolution of the gas radiation solver was evaluated by increasing the number of radiation angles from 60 to 100 and 168. As a result, the MLR and HRR showed only negligible alterations, whereas the simulation time increased considerably.

Notwithstanding the observed deviations, the 1-mm grid resolution and 60 control angles were found to serve as a reliable modeling choice for this study on accounts of acceptable conservation of main pyrolysis features and acceptable computational cost.

The sensitivity of PMMA pyrolysis models to their input parameters has been widely studied in the literature, e.g., [13,46,60]. Chaos [60] investigated the dynamic sensitivities of MLR to PMMA material properties under 25 kW m^{-2} and 100 kW m^{-2} heat fluxes. He found out that the responses of the PMMA MLR were qualitatively similar at different irradiation levels. Chaos observed a

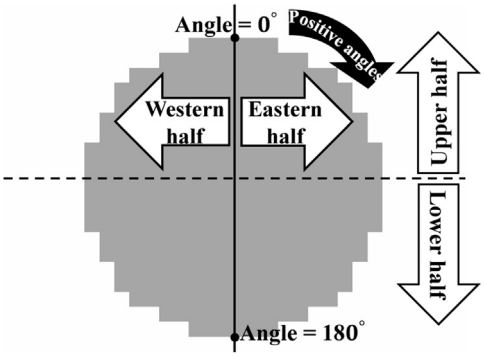

Fig. 11. Geometrical definitions on each PMMA rod.

small positive response for conductivity (higher conductivity leads to higher MLR), a moderately negative response for the specific heat, a relatively large positive response for emissivity, zero dependency on the absorption coefficient, and a relatively large negative response to the heat of reaction.

Here, we varied the condense phase parameters k, c, ϵ, κ, and H_r by $\pm 20\%$. We found only small sensitivity to the variation of the conductivity (Fig. 10(b)) and small sensitivity to the absorption coefficient (Fig. 10(e)), as it was the case with [60]. This implies that the major part of the heating, which leads to evaporation, occurs at the surface of the shrinking PMMA. Increasing the specific heat (Fig. 10(c)) or the heat of reaction (Fig. 10(f)) leads to higher demand of energy for the material to reach the decomposition temperature, thus decreasing the pace and amplitude of the MLR. Decreasing these two parameters by 20% speeds up the decomposition such that the model result would fall out of the uncertainty bounds. These sensitivites are also in line with [60].

Increasing the emissivity leads to higher net absorption of the external heat flux and faster heating of the material, thus speeding up the MLR (Fig. 10(d)). Same observation was made in Chaos [60]. While the 20% increment of emissivity makes the MLR fall outside the experimental uncertainty band, the result obtained with 0.8ϵ is still mostly within the uncertainty bounds.

As explained in Section 3.2 the convective heat fluxes are calculated using empirical correlations with a characteristic length scale $L = 0.1$ m. To assess the model sensitivity to the convective heat transfer calculation, one simulation was performed with a constant heat transfer coefficient of 10 W/(m^2 K) at all surfaces, as suggested in Vermesi et al. [13], Lautenberger and Fernandez-Pello [39], Bal and Rein [40], and another simulation with characteristic length scale equal to the rod diameter, $L = 0.02$ m. Neither simulation led to significantly different MLR or HRR.

5.4. Shape change

This section qualitatively compares experimental and numerical results for the deformation of the PMMA rods. Videos recorded by the thermal camera were colored with arbitrary palettes that were able to provide a clear visualization of the solid cross-section evolution. Snapshots of the video were exported from the desired moments of the experiments. The simulated rod shapes were visualized at the corresponding times by extracting slices of solid cell volume ratio ϕ_s, defined in Eq. (10). This quantity varies in the range of $0 \leq \phi_s \leq 1$, conveying the ratio between the volume of the remaining solid virgin material in a computational cell, V_s, and the volume of the cell itself, V_c.

Before further continuation, a few geometrical definitions are required for clarity. Figure 11 represents these definitions on the surface of a rod, where it is divided into eastern, western, upper, and lower halves. A polar coordinate system is designated to the eastern circumference of the rod such that the top point is assigned to 0°, and the lowest point denotes 180°.

Figure 12 illustrates a sequence of rod shapes for the single rod gasification case. The experimental snapshots on the left show how the rod cross-section shrinks over time. The shrinkage is much faster from the top to bottom than from the sides toward the center of the rod. Assuming that the rod cross-section is only changed due to the material consumption by thermal decomposition, we can conclude that the decomposition rate is higher on the top surface than on the sides. Likewise, the solid cell volume ratio results on the right side of Fig. 12 show the same trend. The reason for the faster evaporation from the top surface is that the conical heater is the principal driver for the decomposition reactions in the gasification experiments. Geometrically, the area of the circumference located close to the top of the shrinking rod has a large view-factor from the conical heater, whereas the other areas of the circumference have lower view-factors.

The cross-sectional degradation pattern for the single rod flaming case is presented in Fig. 13. The experimental image at 53 s from the start of the test shows how the flame has just ignited on the rod top surface and covers roughly the upper half of the rod. At 100 s, the flame has spread down the rod surface and covers the entire rod, except for a small region of the rod end, close to the sample holder. Experimental images from 200 s onward disclose an elliptic shape for the condensed phase, indicating an equal or higher rate of degradation at the sides of the rod than from top to bottom. This distinct difference from the gasification test (Fig. 12) owes to the increased heat flux at the sides of the rod due to the presence of the flame. This effect will be quantified in the next section. The sequence of predicted solid cell volume ratios on the right side of Fig. 13 shows that the numerical model reproduces the shape and rate of shrinkage. The good accuracy of shrinkage prediction indicates that the modeled combustion physics establishes an adequate energy balance in the vicinity of the condensed phase.

Figure 14 provides a sequence of recorded and predicted cross-section images from the five rods gasification experiment. During the experiments, some PMMA melting was observed from the onset of tests, and the melting became more severe as time passed. At about $t = 200$ s, small droplets of molten PMMA began rolling down the cross-sectional area of the rods. Throughout most of the course of the test, the droplets evaporated in the vicinity of the rod but starting from about $t = 1000$ s, a few droplets started falling off the sample holder, and more importantly, small remnants of the outermost rods began disintegrating and tumbling down as well. Most test repetitions continued approximately 100 s more and then seized before disintegrated parts fell down completely. The melting, dripping, and disintegration phenomena were not included in the CFD modeling.

The experimental sequence in Fig. 14 shows the development of a ∪-shape trend of shrinkage, indicating a faster rate of degradation at the center than on the outermost rods. The ∪-shape trend can be explained by two key factors. Firstly, it is partly due to the decline of the incidence heat flux on the sample when moving from the center toward outer regions, as explained in Section 4. Secondly, the view angles from which the two outermost rods perceive the heater radiation poses a significant effect on their shape of degradation. The local heater-to-sample view factor is lower on the eastern half of the rightmost rod than on the western half, and this makes the incident flux distribution uneven on the surface of the rightmost rod. The uneven flux, in turn, leads to an inclination of the active pyrolysis plane when the rod degrades.

The model demonstrates a favorable competence for the reproduction of the ∪-shape trend and preserves most of the degradation features. At this stage, we can also conclude that the 2D

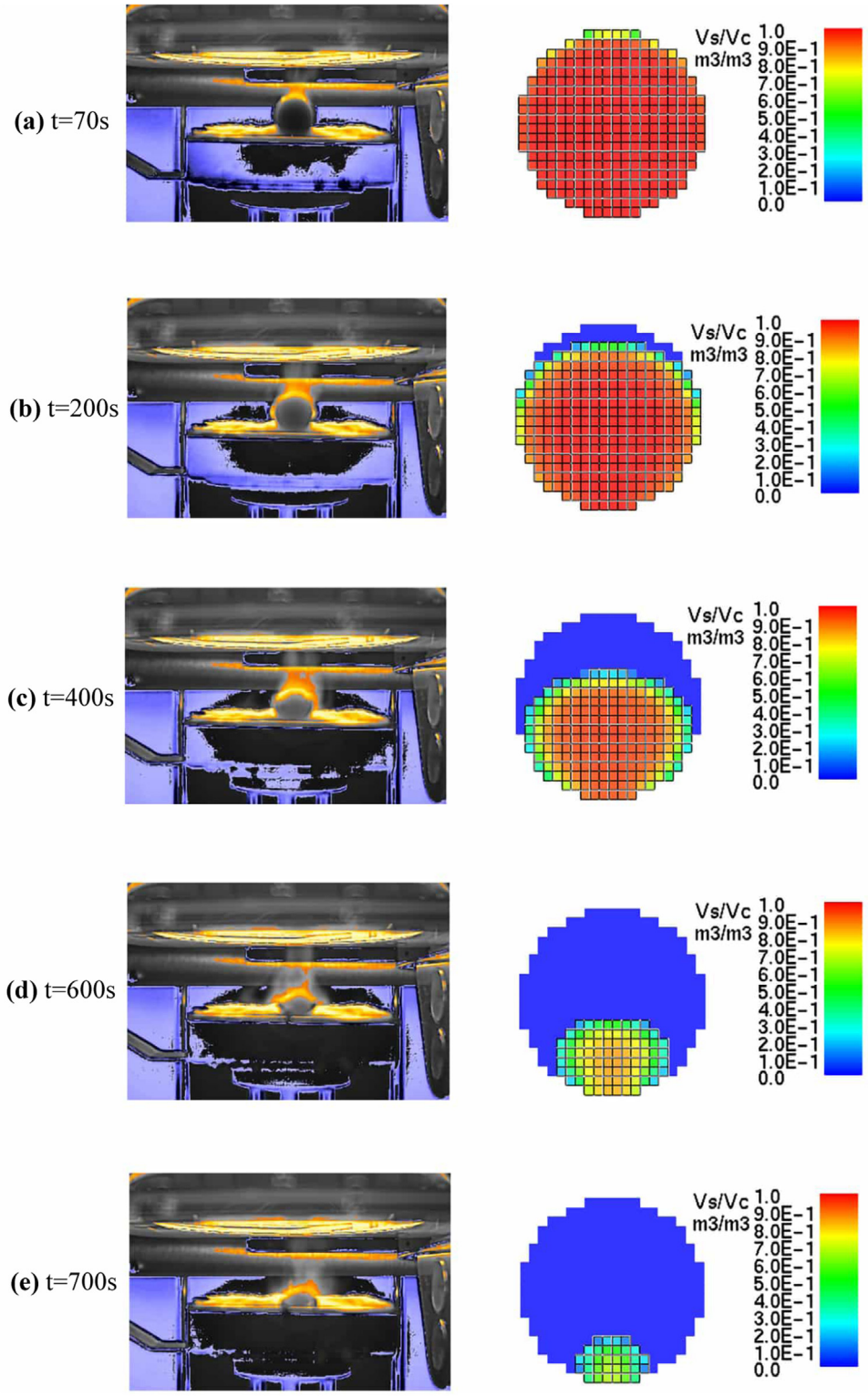

Fig. 12. Comparison of experimental (left) and numerical (right) shapes of the sample cross-section at different times of the single rod gasification experiment. Experimental colors are arbitrary.

modification performed on the geometry of the cone, discussed in Section 4, has not disturbed the overall radiation characteristics of the conical heater. In other words, the process of employing a vertical 2D plane cut from the original 3D cone, and then excluding 12 mm of the elements from both sides of the 2D heater to ensure the correct horizontal flux distribution on top of each rod, maintains the essential spatial and angular intensity distributions.

Finally, the cross-sectional comparison of the experimental and model results for the five rods flaming case is presented in Fig. 15. The flame initiates at the top of rods and then travels downward, covering the outermost rods at approximately 100 s. The degradation trend is opposite to the gasification case, now showing a ∩-shape profile on the top of samples. This time, no dripping or material disintegration was observed in the experiment. The faster

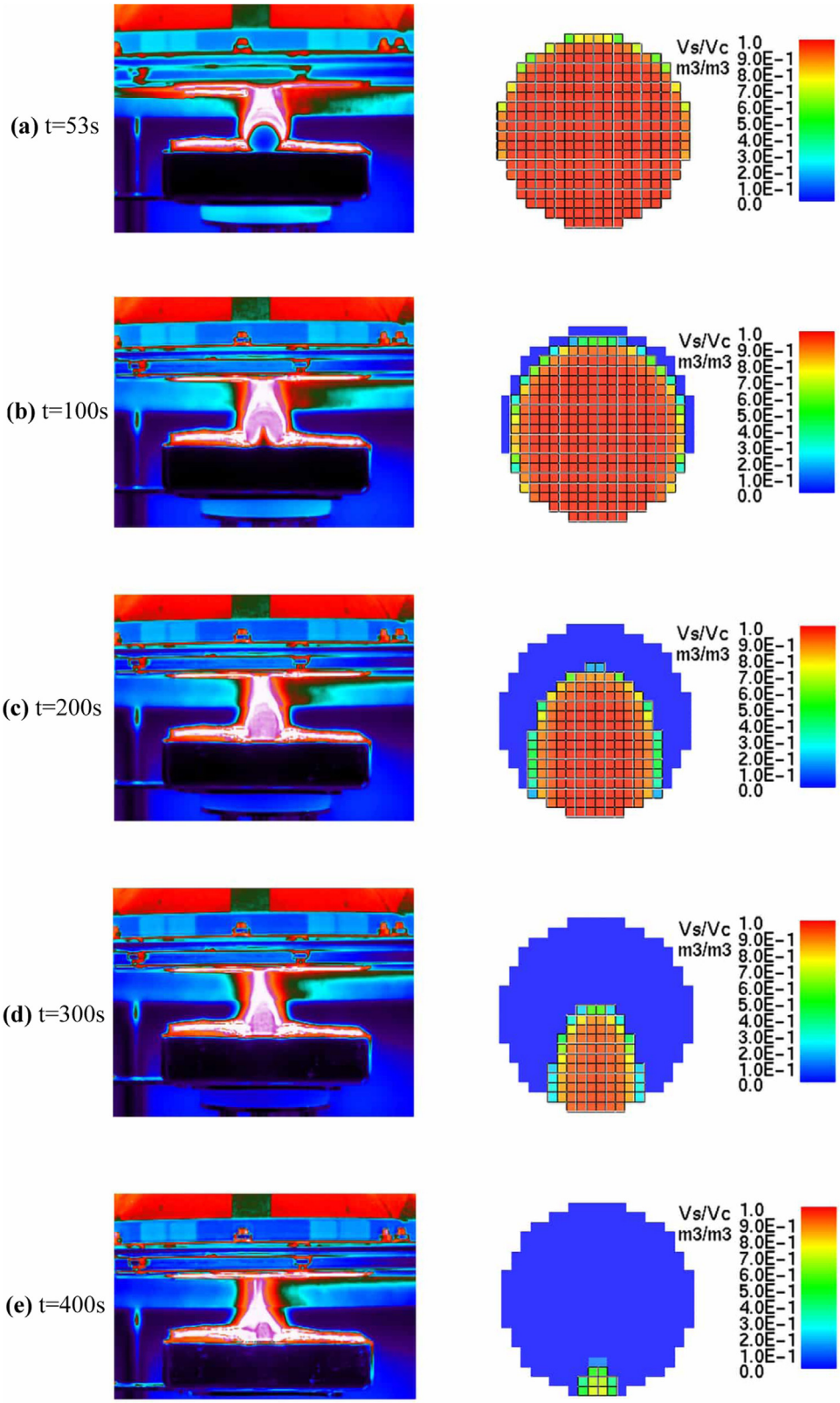

Fig. 13. Comparison of experimental (left) and numerical (right) shapes of the sample cross-section at different times of the single rod flaming experiment. Experimental colors are arbitrary.

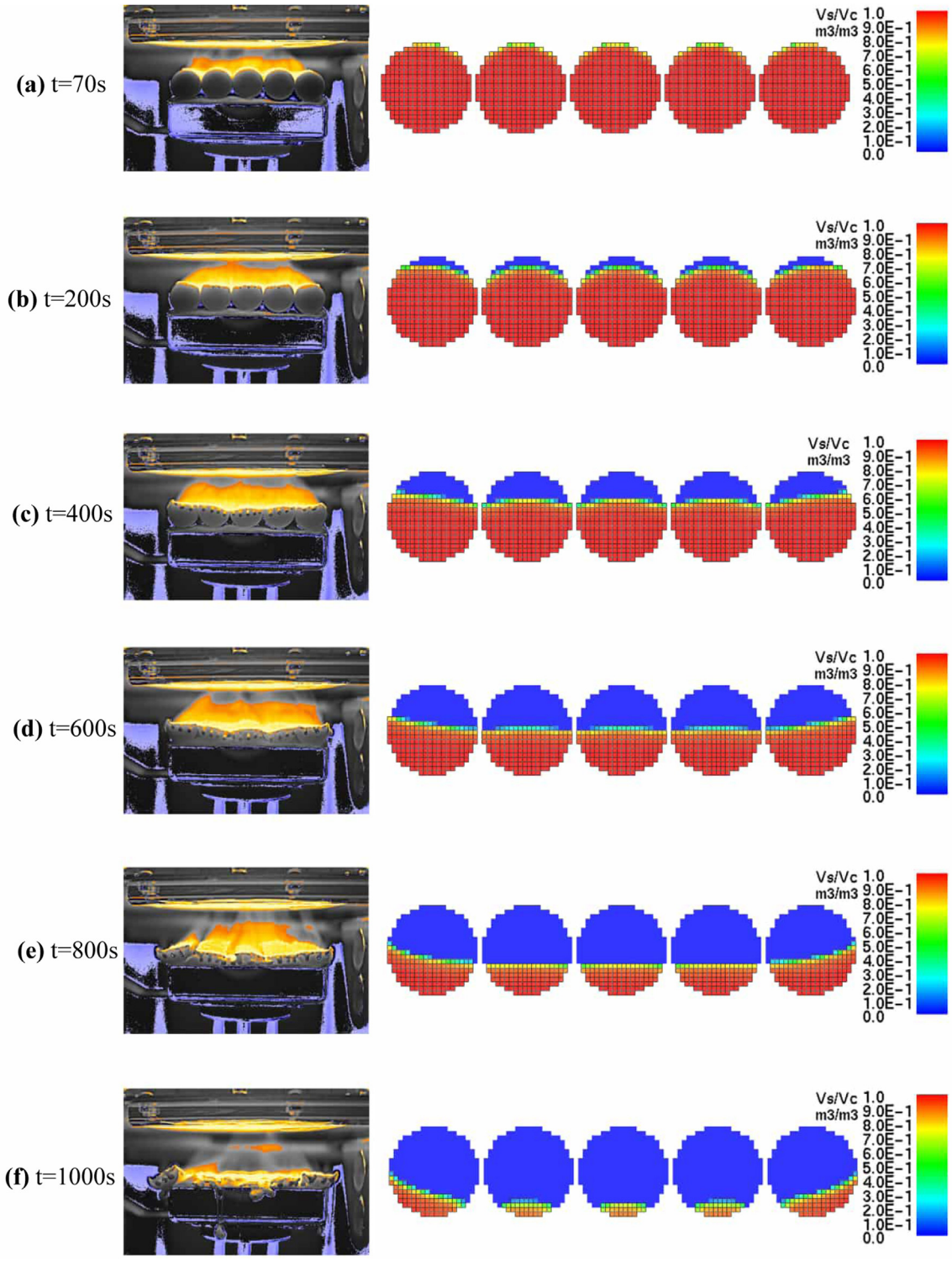

Fig. 14. Comparison of experimental (left) and numerical (right) shapes of the sample cross-section at different times of the five rods gasification experiment. Experimental colors are arbitrary.

degradation of the outermost rods is a consequence of the increased heat transfer at the outermost rods due to the presence of the flame. For the almost entire duration, flame covers the eastern half of the rightmost rod, but the adjacency of its western half to the neighboring rod may not allow flame propagation between two rods. Hence, the eastern half of the rightmost rod receives a higher portion of the local flame-induced heat. The same assertion stands for the western half of the leftmost rod. In addition, the outermost rods burn away faster than the three inner rods. This can be justified by the larger total surface exposed to the flame-induced heat.

The numerical results on the right side of Fig. 15 indicate that the model replicates both the ∩-shape evaporation trend and the faster burn-away of the outermost rods. The qualitative accordance between the numerical and experimental cross-sections can be seen as a sign of the model's capability to reproduce the combustion-induced heat transfer to the surface of the condensed

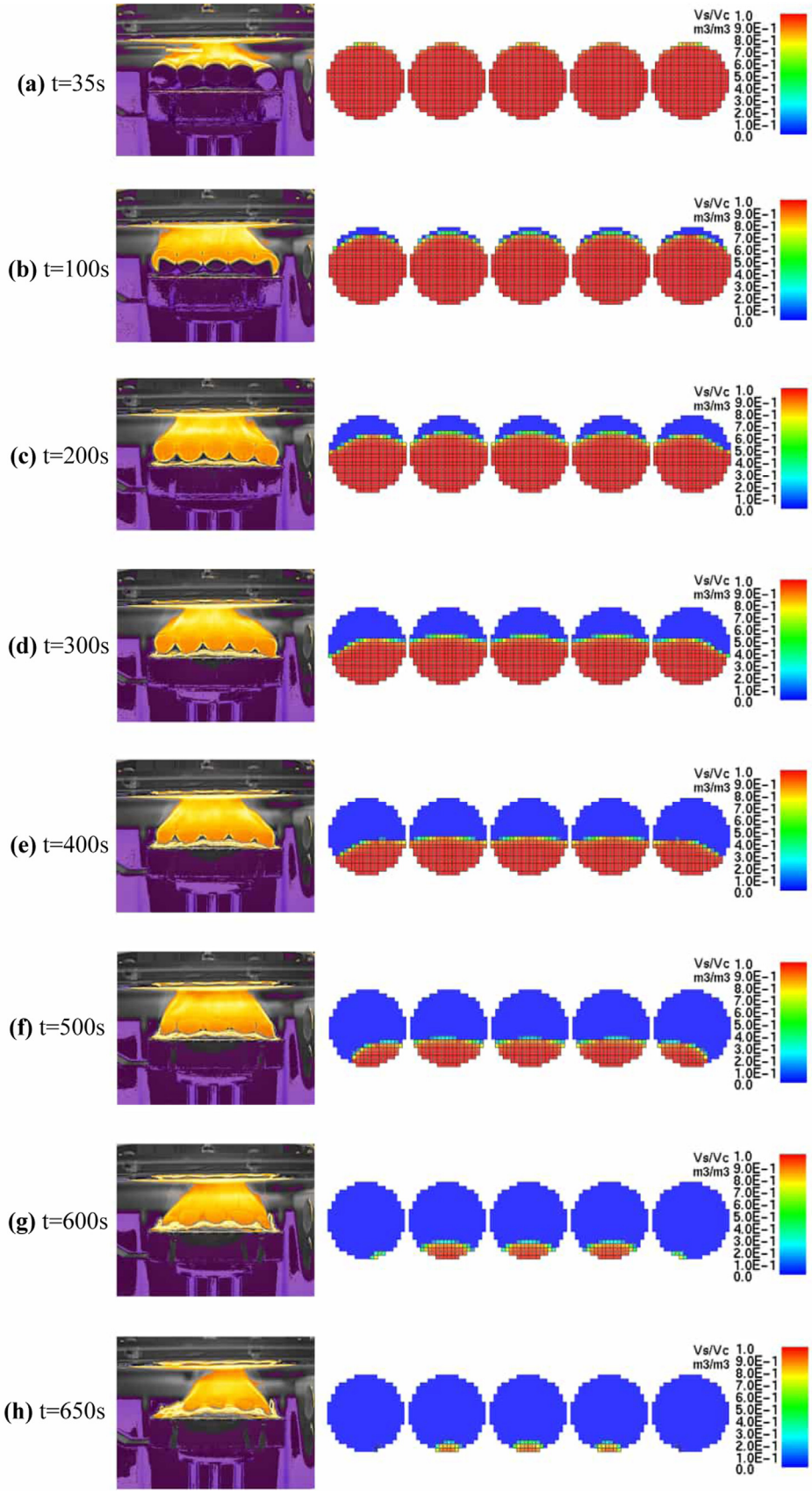

Fig. 15. Comparison of experimental (left) and numerical (right) shapes of the sample cross-section at different times of the five rods flaming experiment. Experimental colors are arbitrary.

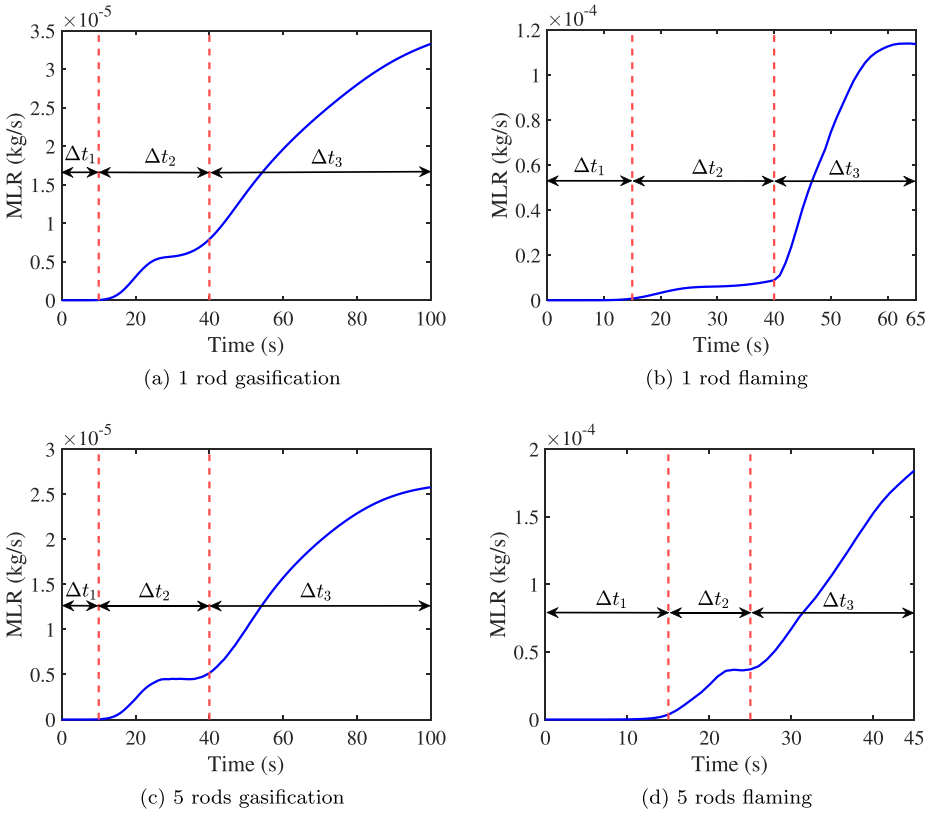

Fig. 16. Definition of averaging time intervals based on the mass loss rate.

phase. Although an under-prediction of total HRR for the current test case was observed in Fig. 9, the local heat transfer effects have been adequately captured.

5.5. Surface quantities

In Section 5.4, the reasons behind the various trends of degradation were qualitatively discussed. In this section, a quantitative analysis is performed on the boundary as well as in the vicinity of the samples. Surface heat fluxes along with 2D snapshots of the relevant gas phase quantities are presented. Only the central and rightmost rods are taken into consideration to facilitate analysis of the underlying physics.

The surface quantities are presented as time averages over three time intervals that were defined to reflect the different stages of the burning process. The first interval, Δt_1, represents a period during which no significant gas generation occurs. The second interval, Δt_2, resembles a moderate MMA evolution, while Δt_3 features an intensified monomer production. These time intervals are shown with the simulated mass loss rates for each scenario in Fig. 16. To avoid ambiguous locations for the wall cells during the averaging process, the data collection was stopped when the first solid cell disappeared from the computation due to the full evaporation, thus defining the end of Δt_3. The gas phase data were taken from the midpoints of the corresponding time intervals.

Extraction of the boundary data from simulations was performed with FDSReader [61] Python tool. As a consequence of the stair-stepping form of the modeled rods, the extracted surface quantities included artificial fluctuations. For the clarity of visualization, the data were smoothed by fitting 7th order polynomials which were found to preserve the vital properties of the original data.

For the single rod gasification case, the time-averaged and spatially smoothed heat fluxes and temperatures along the sample surface are shown in Fig. 17 with separate sub-figures for the three time intervals. As there is no flaming, the top point (0°) of the rod is continuously exposed to the 50 kW m^{-2} incident radiative heat flux, and the irradiation decays with the angular position, being zero at the bottom of the rod (180°). The convective heat flux is negative (cooling) at the upper side of the rod and positive at the lower half, but the magnitude is much smaller than the radiative counterpart, except for the bottom of the rod where two fluxes are of similar magnitude. The positive convection flux is caused by the air stream flowing over the surrounding substrate, fixed at 450 °C temperature, as shown by the continuum temperature slices at the right-hand side of Fig. 17.

The surface temperature continues rising throughout the course of time, especially for angular positions from 0° to 135°. The highest surface temperatures are seen between 0° and 30°. During Δt_3, surface temperature has exceeded 360 °C, the onset of the DTG mass loss (Fig. 2(b)).

The simulated single rod flaming test (Fig. 18) shows similar behavior during the first two time intervals, i.e., when the rod has not yet ignited. The flaming and gasification plots are not identical, though, because the time intervals themselves are slightly different. The flame ignites at the beginning of the Δt_3, as shown by the rightmost figures visualizing the predicted HRR per unit volume (HRRPUV) of the combustion reaction. Ignition increases the incident radiative flux between Δt_2 and Δt_3, mainly at the upper half of the rod (angular positions between 0° and 90°), where the increase is about 15 kW m^{-2}. Correspondingly, the convective heat flux holds a similar form as in the gasification case until the time of ignition, after which significant convective heating takes place on the sides of the rod (angular positions between 60° and 120°). The rise of the radiative flux on the top together with the

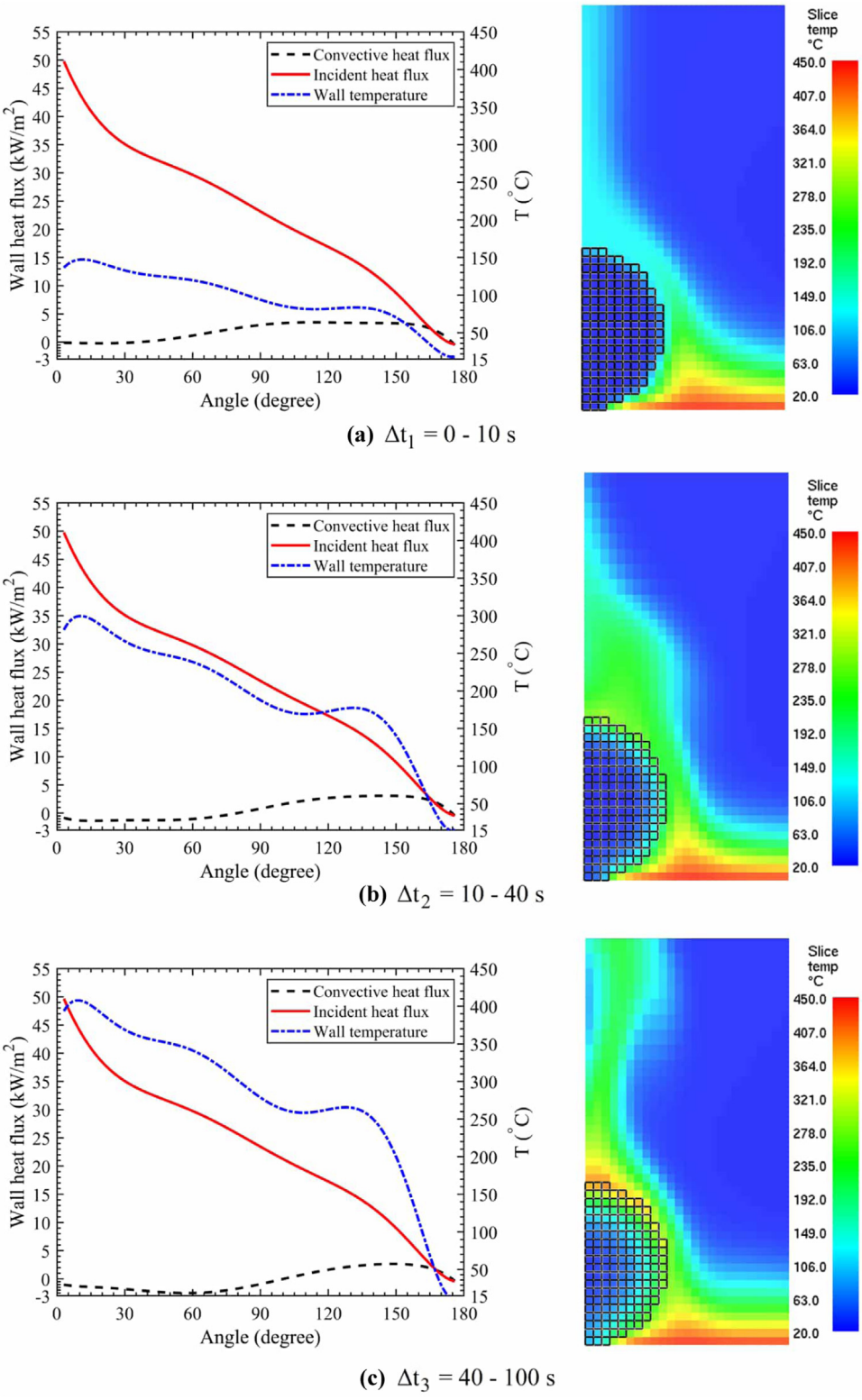

Fig. 17. Simulated heat fluxes and temperatures at the sample surface (left) and continuum temperatures (right) at three time intervals of the single rod gasification test. Surface data on the left are time-averaged over the intervals, while contours represent the results at the midpoint of the time intervals. Gas temperature range is limited to 450 °C to resolve the early stage details.

convection on the sides leads to a nearly flat surface temperature distribution between 0° and 90° in Δt_3. The onset temperature of degradation has been exceeded in positions 0 to 120 degrees. This explains the relatively equal paces of top-to-bottom and sides-to-center shrinkage noticed earlier in Fig. 13. Furthermore, the sequence of temperature slices confirms an almost identical penetration rate of conduction heat in the vertical and horizontal directions.

As to the five rods gasification test case, Fig. 19 presents surface data and slices of temperature for the central and rightmost

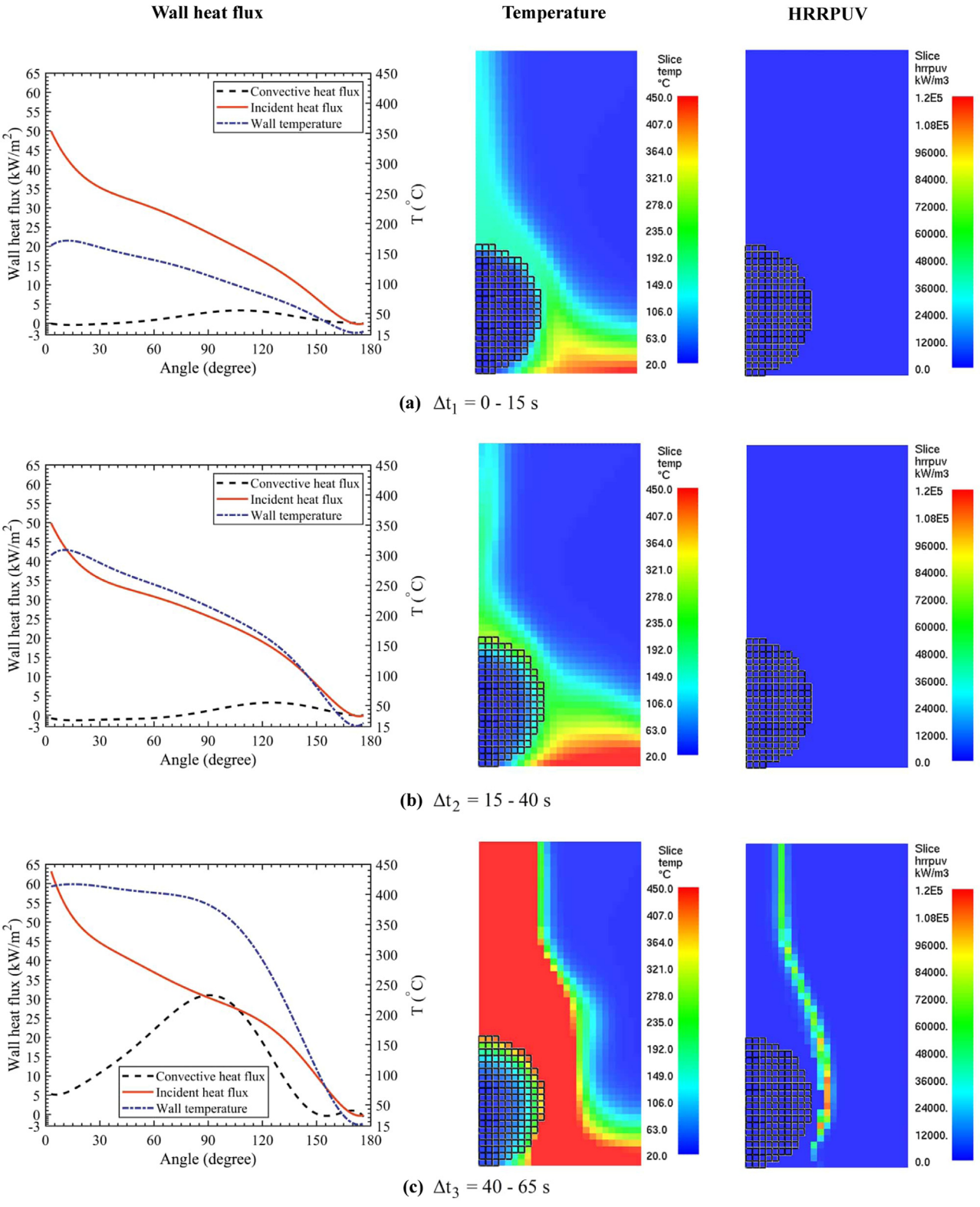

Fig. 18. Simulated heat fluxes and temperatures of the sample surface (left), continuum temperatures (middle), and continuum HRR per unit volume (right) at three time intervals of the single rod flaming test. Surface data on the left are time-averaged over the intervals, while contours represent the results at the midpoint of the time intervals. Gas temperature range is limited to 450 °C to resolve the early stage details.

rods. Similar to the single rod gasification case, the incident heat fluxes remain almost unchanged throughout the course of simulation time. The angular distributions, in turn, show much steeper decay with the angular position. For the central rod, this is caused by the shadowing effect from the neighboring rod, and the reason behind the fast decay on the rightmost rod is the significant reduction of the radiation view-factor of the cone heater on the eastern circumference of the rod. In the same manner as the single rod case, the convective heat transfer is practically insignificant, except for a slight convective cooling on the eastern half of

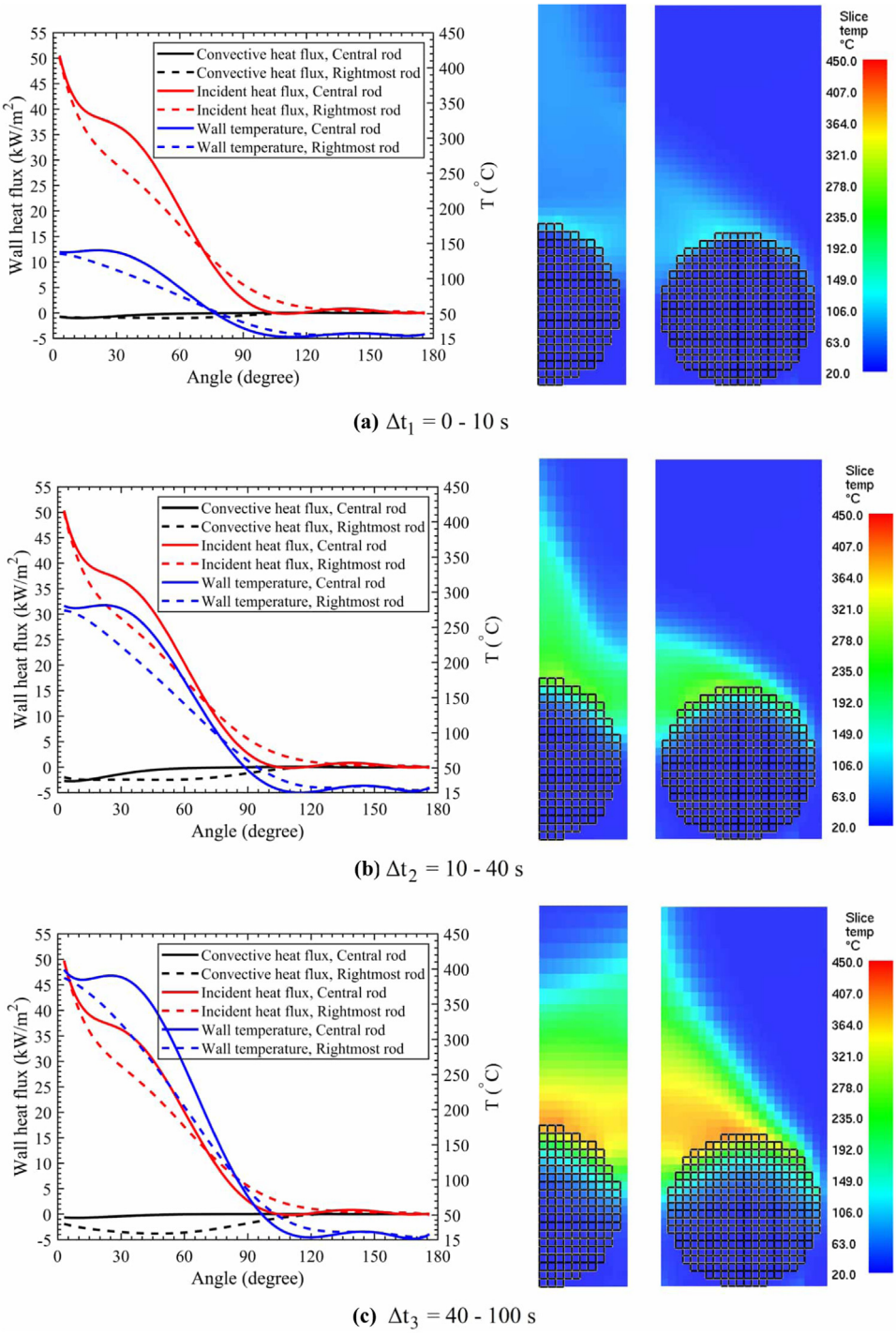

Fig. 19. Simulated heat fluxes and temperatures of the sample surface (left) and continuum temperatures (right) at three time intervals of the five rods gasification test. Surface data on the left are time-averaged over the intervals, while contours represent the results at the midpoint of the time intervals. Gas temperature range is limited to 450 °C to resolve the early stage details.

the rightmost rod for angles between 0° and 90°, most visible in Δt_3. This is due to a free stream of cold ambient Nitrogen from the exteriors toward the rightmost rod, possessing a large momentum in the proximity of the mentioned circumferential angles.

The surface temperatures increase between Δt_1 and Δt_3, but only on the upper halves of both rods. The circumferential regions exceeding the 360 °C threshold in Δt_3 (Fig. 19(c)) are limited between 0° and 45° in the central rod, and between 0° and 10° at the eastern half of the rightmost rod. The relatively higher temperatures at the western half of the rightmost rod are also apparent in the continuum temperature slices of Fig. 19. These circumstances will then lead to the ∪-shape trend of the sample shrinkage at later times, as discussed in Section 5.4.

Figure 20 presents surface heat fluxes and temperatures, along with slices of continuum temperature and HRRPUV for the five rods flaming case. As the flame has not yet ignited at Δt_1, the incident heat fluxes closely resemble those of the five rods gasification case. Following the flame initiation at the beginning of Δt_2 (Fig. 20(b)), the incident fluxes show only a slight increase on the

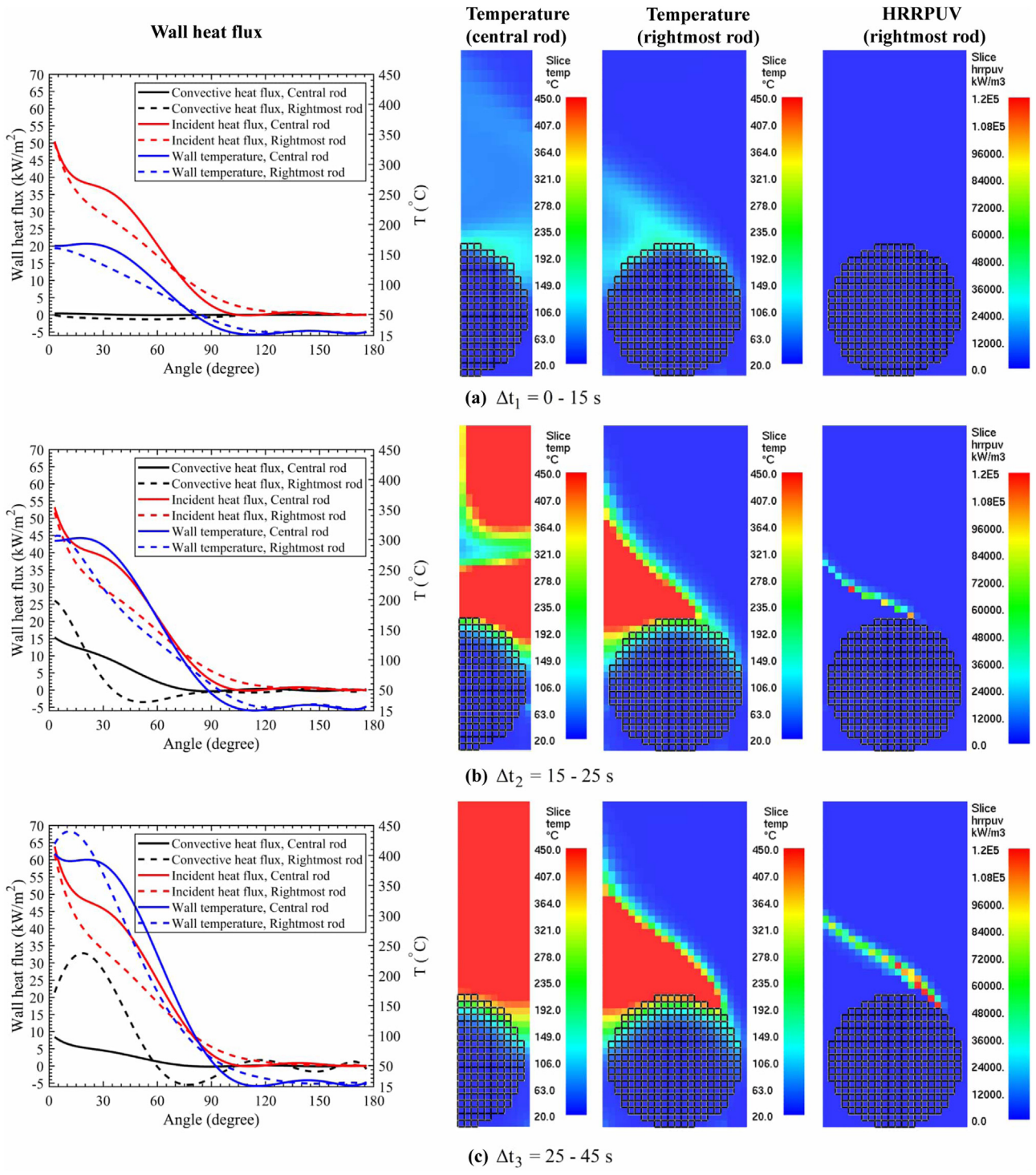

Fig. 20. Simulated heat fluxes and temperatures of the sample surface (left), continuum temperatures (middle), and continuum HRR per unit volume (right) at three time intervals of the five rods flaming test. Surface data on the left are time-averaged over the intervals, while contours represent the results at the midpoint of the time intervals. Gas temperature range is limited to 450 °C to resolve the early stage details.

upper halves of both rods. During Δt_3, the 15 kW m^{-2} increase can again be observed on the top of both rods.

The flame can be seen to increase the convective heat flux on the rightmost rod much more than on the central rod. In the early phase of the flaming, up to 15 kW m^{-2} convective heating can be observed on the top of the central rod, but the flux is reduced when the surface temperature increases. On the rightmost rod, the convection can be divided into two zones: a flame-induced heating zone on the top, and a moderate convective cooling zone just below the flame lower edge, where a free stream of cold ambient air impinges the rod surface. In Fig. 20(b) for instance, the convective heating appears between 0° and 30° and convective cooling from 30° to 80°. As the flame (HRRPUV) travels down the eastern half of the rod between Fig. 20(b) and (c), the convective heating

zone expands from 30° to about 60°. Simultaneously, the cooling zone moves down on the rod. Consistent effects are also visible in the surface temperature distributions. The ∩-shape trend of the sample shrinkage in Fig. 15 can be seen as a consequence of the higher convective heat flux on the first and last rods.

Effects of the cylindrical fuels' tight alignment in flaming cone calorimetry have been experimentally studied for electrical cables [29,30] and wood rods [23]. Magalie et al. [30] and Meiner et al. [29] conclude that the tight layout has effects on the heat transfer and associate them partly with the shadowing effect and partly with some poorly recognized convective flux alterations because of rods adjacency. Lin et al., on the other hand, present a hypothesis that the tight layout significantly reduces the region of convective cooling in comparison to the cooled surface of a single rod [23]. The current study confirmed the severe shadowing effect on the lower halves of the inner rods (Figs. 19 and 20). Moreover, in both flaming cases, it was conspicuous that the flame-induced convective heating dominates over the convective cooling, albeit only after ignition. Furthermore, comparing the convective heat flux on the single flaming rod in Fig. 18(c) against the flux on the central rod of the five flaming rods (Fig. 20(c)), it is evident that the amount of flame induced convective heating has drastically reduced for the tightly surrounded central rod. In other words, this study does not support the hypothesis of reduced convective cooling in tight alignment, as suggested in Lin et al. [23], but demonstrates a reduction of the flame-induced convective heating instead. Although the shorter ignition time of the five rod case would, indeed, support the hypothesis of reduced cooling, this study indicates that the shorter ignition delay simply follows from higher mass flow of fuel gas, reaching the lower flammability limit at the pilot position at earlier time.

6. Conclusion

Although the cone calorimeter, as defined by ISO 5660-standard, is meant for studying the flammability of solid fuels with slab geometry, the need to investigate the flammability of non-planar objects, such as electrical cables and bio-fuel particles, has led to its applications with cylindrical objects. In the absence of a detailed understanding of the heat exposure in such geometrical conditions, both the interpretations of experiments and the efforts to develop computational pyrolysis models have mapped the sample into a rectangular surrogate volume. Such a simplification fails to take into account the inherently nonhomogeneous nature of the radiative and convective heat fluxes, possibly leading to strong compensation effects during model parameter estimation and endangering the model accuracy in engineering applications.

In this study, we introduced a new computational model for the combustion simulation of cylindrical objects under radiative heat exposure, such as the cone calorimeter, validated the model through experiments with non-charring cylindrical objects, and extracted detailed thermodynamic information from the sample surface to support future studies. Thermal decomposition of black PMMA rods was experimentally analyzed under 50 kW m^{-2} nominal irradiation in both non-flaming (gasification) and flaming conditions. Two sample layouts, namely single rod and five rods, were utilized.

The development of the PMMA rods' cross-section shape was monitored experimentally using a thermal camera. A steep top-to-bottom degradation rate was observed in the single rod gasification test, whereas the single rod flaming test revealed almost equal top-to-bottom and sides-to-center shrinkage rates. In the five rods experiments, a ∪-shape trend of shrinkage was observed under gasification conditions, while that of flaming condition bore a ∩-shape trend.

The computational model was validated quantitatively by comparing the predicted mass loss and heat release rate histories against the experimental data. Model predictions were mostly within the bounds of the experimental uncertainty, correctly capturing the ignition times and the shapes of the burning rate histories. Both the experiments and simulations indicated a shorter ignition delay time for the five rods case in comparison to the single rod case, consistently with the study of Lin et al. [23].

The highest modeling uncertainties were observed while simulating the five rods flaming experiment, where the model failed to reproduce the decreasing trend of burning and under-predicted the total HRR by 16%. The refinement of the CFD resolution mainly improved the accuracy of the burnout phase. Regarding the sample cross-sections, the model successfully captured the qualitative differences between the gasification and flaming conditions. It was concluded that the thermal conditions were adequately reproduced and the simulations can be used as a reliable source of detailed thermodynamic information for such experiments.

While the experimental results revealed the dynamics of non-charring cylindrical polymers pyrolyzing and combusting under one-sided radiation exposure, the numerical results showed how the cylindrical sample geometry leads to more complex spatial and angular profiles of the convective and radiative heat fluxes than what can be observed over flat samples. The change of these thermophysical profiles upon ignition was also unmasked. These information will enable the use of simplified, fast engineering models for the same problem, as the heat fluxes can be accurately prescribed. Subsequently, the fast models can be applied for optimization of pyrolysis model parameters of cylindrical samples.

The analysis of the simulated heat flux distributions shed light on the reasons behind the different shrinkage patterns. Despite the observed increase of the sample substrate's surface temperature, the external radiation remained dominating on the samples' top surface. The shadowing-effect because of the abutting rods was observed with the five, tightly aligned rods, which was in line with the hypotheses presented in Magalie et al. [30] and Meinier et al. [29].

The flames were found to induce about 15 kW m^{-2} increase of incident radiative flux on the rod tops. The induced convective heat fluxes were up to 30 kW m^{-2} on the sides of the single or outmost rods, and up to 25 kW m^{-2} on the top surfaces. The convective heating accounts for the increased rate of sides-to-center shrinkage in the single rod case and the intensified pace of degradation on the outermost rods in the five rods case. In general, the convective cooling was low in magnitude, and it was not affected by the rod alignment (single vs. five rods), which is against the hypothesis of Lin et al. [23].

Although the current framework was applied to model non-charring rods, it has the potential of further expansion to more complex cylindrical samples such as electrical cables and nonhomogeneous bio-based fuels. Future works will concentrate on including additional mechanisms like charring, melting, and swelling, which can significantly contribute to the burning of more complex fuels.

Declaration of Competing Interest

The authors declare that they have no known competing financial interests or personal relationships that could have appeared to influence the work reported in this paper.

Acknowledgements

This study has been funded by the State Nuclear Waste Management Fund (VYR). The authors would like to acknowledge Aleksi Rinta-Paavola for help when conducting cone calorimeter

experiments, and Rahul Kallada Janardhan for assisting with thermal imaging. This work made use of Aalto University Bioeconomy Facilities when performing TGA measurements. The authors wish to acknowledge CSC - IT Center for Science, Finland, for computational resources.

Appendix A. 3D simulation of single rod flaming case

A quarter of the test chamber was modeled with a $92 \times 92 \times 297.5$ mm^3 domain. The model was limited to one quarter to reduce the 3D computational cost, and justified by the observed laminar nature of the flow in the sample's vicinity. The $y = 0$ and $x = 0$ planes were set as mirror boundaries to enforce symmetry and the other outer boundaries were open. The original cone geometry in Fig. A.1(a) was utilized and the heater temperature re-adjusted to achieve 50 kW m^{-2} incident flux on the top of the rod. The mesh resolution was equivalent to the 2D models, with $1 \times 1 \times 1$ mm^3 cells in the lower part of the domain and $1 \times 1 \times 1.875$ mm^3 above. The domain was divided into 15 meshes, each assigned to a separate MPI process. To enable a meaningful comparison with the 2D model, the 3D simulation was run for a few tens of seconds after ignition, i.e., until $t = 170$ s. With the current setup, the simulation was about 10 times slower than with the 2D model.

Figure A.1 (b) compares the simulated incident heat flux distributions at rod center, averaged over $t = 0$–15 s. The 2D incident flux is slightly higher than in the 3D simulation on top of the cylinder, whereas an increasing deviation can be observed while moving down the cylinder. The difference on the top is a result of less accurate heater calibration in 3D. The steeper reduction of the heat flux with angle in 3D, in turn, is a direct consequence of different heater geometries; each point on a rod surface sees the 2D heater as two infinitely long elements, while the view factors from a 3D cone to cylinder decreases quickly with angle.

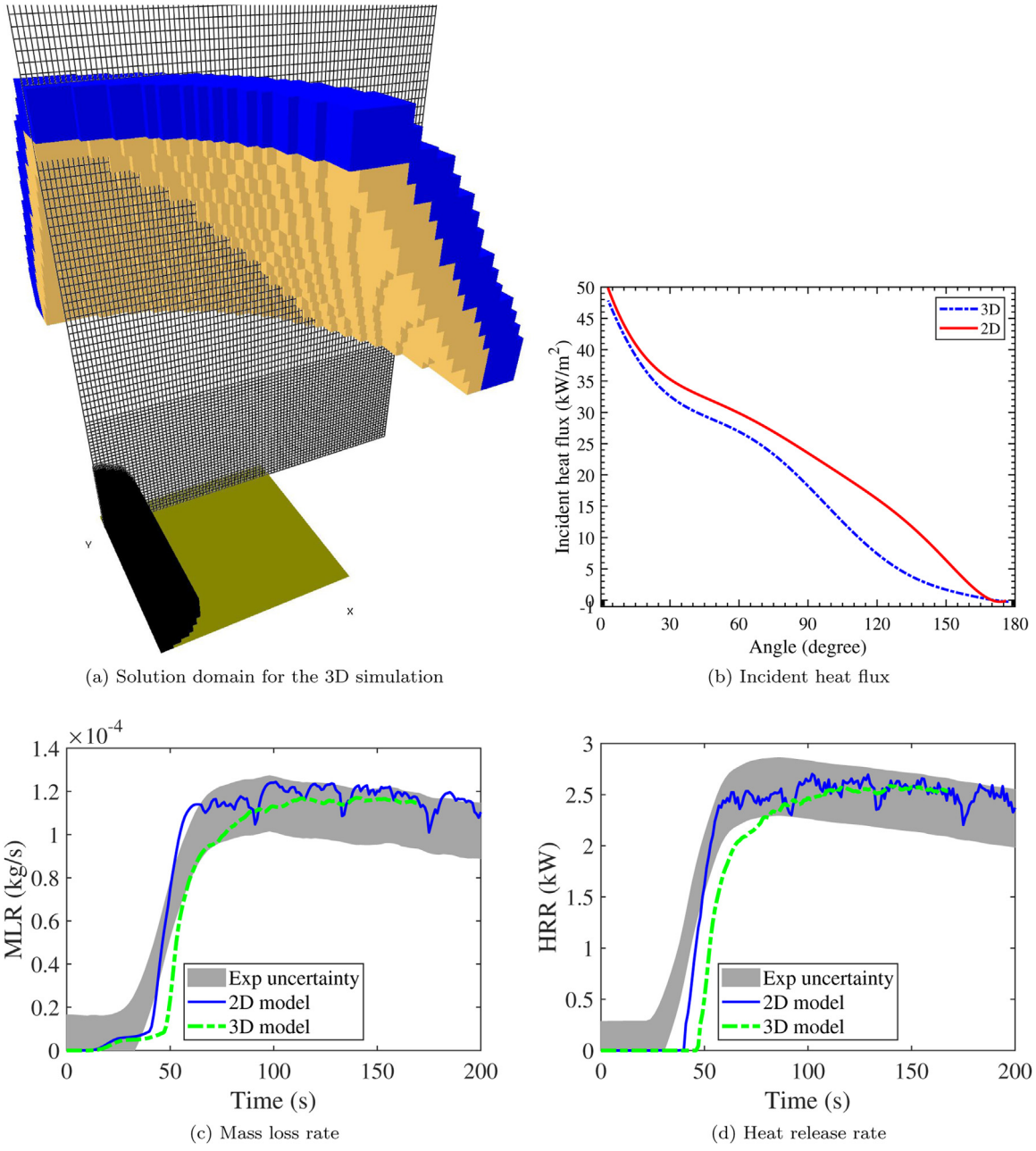

(a) Solution domain for the 3D simulation

(b) Incident heat flux

(c) Mass loss rate

(d) Heat release rate

Fig. A.1. 3D simulation domain and comparisons of 3D and 2D predictions for the incident heat flux, MLR, and HRR. The 3D simulation was performed only until 170 s.

Figure A.1 (c) and (d) compare the MLR and HRR from 2D and 3D simulations. The 3D results are multiplied by a factor of four to account for the quarter domain. The ignition time in the 3D model is about 15 s longer than in the experiments and 7 s longer than in the 2D model. These differences are a consequence of the lower incidence flux. After ignition, the MLR and HRR curves from the two simulations are very close to each other, thus demonstrating the adequacy of the 2D model as a research tool for the current purpose.

References

[1] S. Tao, J. Fang, Y. Meng, H.R. Shah, L. Yang, Ignition risk analysis of common building material cylindrical PMMA exposed to an external irradiation with in-depth absorption, Constr. Build. Mater. 251 (2020) 118955.
[2] M. Ahrens, Home Structure Fires: National Fire Protection Association, Fire Analysis and Research Division Quincy, MA, 2013.
[3] O. Keski-Rahkonen, J. Mangs, Electrical ignition sources in nuclear power plants: statistical, modelling and experimental studies, Nucl. Eng. Des. 213 (2–3) (2002) 209–221.
[4] F. Jia, M. Patel, E. Galea, A. Grandison, J. Ewer, CFD fire simulation of the Swissair flight 111 in-flight fire—Part 1: prediction of the pre-fire air flow within the cockpit and surrounding areas, Aeronaut. J. 110 (1103) (2006) 41–52.
[5] M. Kikuchi, O. Fujita, K. Ito, A. Sato, T. Sakuraya, Experimental study on flame spread over wire insulation in microgravity, Symp. (Int.) Combust. 27 (1998) 2507–2514. Elsevier
[6] A.F. Osorio, K. Mizutani, C. Fernandez-Pello, O. Fujita, Microgravity flammability limits of ETFE insulated wires exposed to external radiation, Proc. Combust. Inst. 35 (3) (2015) 2683–2689.
[7] S.L. Olson, P.V. Ferkul, Microgravity flammability boundary for PMMA rods in axial stagnation flow: experimental results and energy balance analyses, Combust. Flame 180 (2017) 217–229.
[8] W.L. Fons, Heating and ignition of small wood cylinders, Ind. Eng. Chem. 42 (10) (1950) 2130–2133.
[9] S. McAllister, M. Finney, Autoignition of wood under combined convective and radiative heating, Proc. Combust. Inst. 36 (2) (2017) 3073–3080.
[10] Reaction-to-fire tests – heat release, 2015, Smoke production and mass loss rate—Part 1: heat release rate (cone calorimeter method) and smoke production rate (dynamic measurement), ISO 5660-1.
[11] J. Li, J. Gong, S.I. Stoliarov, Gasification experiments for pyrolysis model parameterization and validation, Int. J. Heat Mass Transf. 77 (2014) 738–744.
[12] J. Li, J. Gong, S.I. Stoliarov, Development of pyrolysis models for charring polymers, Polym. Degrad. Stab. 115 (2015) 138–152.
[13] I. Vermesi, N. Roenner, P. Pironi, R.M. Hadden, G. Rein, Pyrolysis and ignition of a polymer by transient irradiation, Combust. Flame 163 (2016) 31–41.
[14] G.T. Linteris, R.E. Lyon, S. Stoliarov, Prediction of the gasification rate of thermoplastic polymers in fire-like environments, Fire Saf. J. 60 (2013) 14–24.
[15] J.D. Swann, Y. Ding, S.I. Stoliarov, Comparative analysis of pyrolysis and combustion of bisphenol a polycarbonate and poly (ether ether ketone) using two-dimensional modeling: a relation between thermal transport and the physical structure of the intumescent char, Combust. Flame 212 (2020) 469–485.
[16] J.D. Swann, Y. Ding, S.I. Stoliarov, Characterization of pyrolysis and combustion of rigid poly (vinyl chloride) using two-dimensional modeling, Int. J. Heat Mass Transf. 132 (2019) 347–361.
[17] J.D. Swann, Y. Ding, S.I. Stoliarov, A quantitative comparison of the pyrolysis and combustion behavior of plasticized and rigid poly (vinyl chloride) using two-dimensional modeling, Fire Saf. J. 111 (2020) 102910.
[18] A. Matala, S. Hostikka, Pyrolysis modelling of PVC cable materials, Fire Saf. Sci. 10 (2011) 917–930.
[19] S. Grayson, P. Van Hees, A. Green, H. Breulet, U. Vercellotti, Assessing the fire performance of electric cables (FIPEC), Fire Mater. 25 (2) (2001) 49–60, doi:10.1002/fam.756.
[20] T.-H. Tsai, M.-J. Li, I.-Y. Shih, R. Jih, S.C. Wong, Experimental and numerical study of autoignition and pilot ignition of PMMA plates in a cone calorimeter, Combust. Flame 124 (3) (2001) 466–480.
[21] C. Brescianini, G. Yeoh, V. Chandrasekaran, R. Yuen, A numerical model for pilot ignition of PMMA in a cone calorimeter, Combust. Sci. Technol. 129 (1–6) (1997) 321–345.
[22] N. Hernández, A. Fuentes, P. Reszka, A. Fernández-Pello, Piloted ignition delay times on optically thin PMMAcylinders, Proc. Combust. Inst. 37 (3) (2019) 3993–4000.
[23] S. Lin, X. Huang, J. Urban, S. McAllister, C. Fernandez-Pello, Piloted ignition of cylindrical wildland fuels under irradiation, Front. Mech. Eng. 5 (2019) 54.
[24] A.W. Coaker, M.M. Hirschler, C. Shoemaker, Rate of heat release testing for vinyl wire and cable materials with reduced flammability and smoke–full-scale cable tray tests and small-scale tests, Fire Saf. J. 19 (1) (1992) 19–53.
[25] M.A. Barnes, P.J. Briggs, M.M. Hirschler, A.F. Matheson, T.J. O'Neill, A comparative study of the fire performance of halogenated and non-halogenated materials for cable applications. Part I tests on materials and insulated wires, Fire Mater. 20 (1) (1996) 1–16.
[26] G. Fontaine, F.-E. Ngohang, L. Gay, S. Bourbigot, Investigation of the contribution to fire of electrical cable by a revisited mass loss cone, Fire Science and Technology 2015, Springer (2017), pp. 687–693.
[27] K.B. McGrattan, A.J. Lock, N.D. Marsh, M.R. Nyden, et al., Cable heat release, ignition, and spread in tray installations during fire (christifire): phase 1-horizontal trays, 2012,
[28] K.B. McGrattan, S.D. Bareham, et al., Cable heat release, ignition, and spread in tray installations during fire (christifire) phase 2: vertical shafts and corridors, 2013,
[29] R. Meinier, R. Sonnier, P. Zavaleta, S. Suard, L. Ferry, Fire behavior of halogen-free flame retardant electrical cables with the cone calorimeter, J. Hazard. Mater. 342 (2018) 306–316.
[30] C. Magalie, C. Anne-Sophie, S. Rodolphe, F. Laurent, G. Emmanuelle, L. Christian, Fire behaviour of electrical cables in cone calorimeter: influence of cables structure and layout, Fire Saf. J. 99 (2018) 12–21.
[31] C. Lautenberger, C. Fernandez-Pello, Generalized pyrolysis model for combustible solids, Fire Saf. J. 44 (6) (2009) 819–839.
[32] K.B. McGrattan, H.R. Baum, R.G. Rehm, A. Hamins, G.P. Forney, J.E. Floyd, S. Hostikka, K. Prasad, Fire Dynamics Simulator–Technical Reference Guide, National Institute of Standards and Technology, Building and Fire Research Laboratory, 2000.
[33] S. Stoliarov, R. Lyon, Thermo-kinetic model of burning for pyrolyzing materials, Fire Saf. Sci. 9 (2008) 1141–1152.
[34] A. Matala, Methods and Applications of Pyrolysis Modelling for Polymeric Materials, VTT Science, vol. 44, VTT Technical Research Centre of Finland Ltd., 2013. Dissertation
[35] S. Hostikka, A. Matala, Modelling the fire behaviour of electrical cables, 20th International Conference on Structural Mechanics in Reactor Technology (SMiRT 20)–11th International Post Conference Seminar on Fire Safety in Nuclear Power Plants and Installations (2009).
[36] A. Matala, S. Hostikka, Probabilistic simulation of cable performance and water based protection in cable tunnel fires, Nucl. Eng. Des. 241 (12) (2011) 5263–5274.
[37] T. Hehnen, L. Arnold, S. La Mendola, Numerical fire spread simulation based on material pyrolysis–an application to the christifire phase 1 horizontal cable tray tests, Fire 3 (3) (2020) 33.
[38] T. Steinhaus, Evaluation of the Thermophysical Properties of Poly (Methylmethacrylate): A Reference Material for the Development of a Flammability Test for Micro-Gravity Environments, Tech. rep., The University of Maryland, 1999.
[39] C. Lautenberger, C. Fernandez-Pello, A Generalized Pyrolysis Model for Combustible Solids, The University of California, Berkeley, 2007 Ph.D. dissertation.
[40] N. Bal, G. Rein, Numerical investigation of the ignition delay time of a translucent solid at high radiant heat fluxes, Combust. Flame 158 (6) (2011) 1109–1116.
[41] J. Li, S.I. Stoliarov, Measurement of kinetics and thermodynamics of the thermal degradation for non-charring polymers, Combust. Flame 160 (7) (2013) 1287–1297.
[42] G.J. Fiola, D.M. Chaudhari, S.I. Stoliarov, Comparison of pyrolysis properties of extruded and cast poly (methyl methacrylate), Fire Saf. J. 120 (2021) 103083.
[43] I.T. Leventon, J. Li, S.I. Stoliarov, A flame spread simulation based on a comprehensive solid pyrolysis model coupled with a detailed empirical flame structure representation, Combust. Flame 162 (10) (2015) 3884–3895.
[44] I.T. Leventon, K.T. Korver, S.I. Stoliarov, A generalized model of flame to surface heat feedback for laminar wall flames, Combust. Flame 179 (2017) 338–353.
[45] T. Hirata, T. Kashiwagi, J.E. Brown, Thermal and oxidative degradation of poly (methyl methacrylate): weight loss, Macromolecules 18 (7) (1985) 1410–1418.
[46] N. Bal, Uncertainty and complexity in pyrolysis modelling, 2012,
[47] M. Ferriol, A. Gentilhomme, M. Cochez, N. Oget, J. Mieloszynski, Thermal degradation of poly (methyl methacrylate)(PMMA): modelling of DTG and TG curves, Polym. Degrad. Stab. 79 (2) (2003) 271–281.
[48] A.A. Ipiña, M.L. Urrutia, D.L. Urrutia, D.A. Portilla, Thermal oxidative decomposition estimation combining TGA and DSC as optimization targets for PMMA, J. Phys. 1107 (2018) 032011. IOP Publishing
[49] I. Leventon, B. Batiot, M. Bruns, S. Hostikka, Y. Nakamura, P. Reszka, T. Rogaume, S. Stoliarov, et al., The maCFP condensed phase working group: a structured, global effort towards pyrolysis model development, ASTM E05 - Symposium on Obtaining Data for Fire Growth Models, ASTM STP1642, American Society for Testing and Materials, 2021.
[50] M.F. Modest, Fundamentals of thermal radiation, Radiat. Heat transf. 1 (2003) 1–29.
[51] W.M. Rohsenow, J.P. Hartnett, Y.I. Cho, et al., Handbook of Heat Transfer, vol. 3, McGraw-Hill New York, 1998.
[52] B.F. Magnussen, B.H. Hjertager, On mathematical modeling of turbulent combustion with special emphasis on soot formation and combustion, Symp. (Int.) Combust. 16 (1977) 719–729. Elsevier
[53] Insulfrax LTX blancket product information sheet, 2021, https://www.unifrax.com/wp-content/uploads/2018/08/U-216.pdf, accessed: 2022-02-25.
[54] S. Hostikka, J. Axelsson, Modelling of the Radiative Feedback from the Flames in Cone Calorimeter, Nordtest, Finland, 2003.
[55] P. Boulet, G. Parent, Z. Acem, A. Collin, M. Försth, N. Bal, G. Rein, J. Torero, Radiation emission from a heating coil or a halogen lamp on a semitransparent sample, Int. J. Therm. Sci. 77 (2014) 223–232.
[56] K.T. Paul, Cone calorimeter: initial experiences of calibration and use, Fire Saf. J. 22 (1) (1994) 67–87.
[57] M.J. Hurley, D.T. Gottuk, J.R. Hall Jr., K. Harada, E.D. Kuligowski, M. Puchovsky,

J.M. Watts Jr., C.J. Wieczorek, et al., SFPE Handbook of Fire Protection Engineering, Springer, 2015.
[58] L. Shi, M.Y.L. Chew, Fire behaviors of polymers under autoignition conditions in a cone calorimeter, Fire Saf. J. 61 (2013) 243–253.
[59] Methyl methacrylate safety sheet, 2021, https://inchem.org/documents/icsc/icsc/eics0300.htm, accessed: 2022-02-25.
[60] M. Chaos, Application of sensitivity analyses to condensed-phase pyrolysis modeling, Fire Saf. J. 61 (2013) 254–264.
[61] FDSReader python tool, 2022, https://github.com/FireDynamics/fdsreader, accessed: 2022-02-25.